12-14-2022

Shape Optimization of Spherical and Cylindrical Bearings Under Pure Squeeze Conditions Using Genetic Algorithms

Vibhav Santhanam
vns4343@rit.edu

Shape Optimization of Spherical and Cylindrical Bearings Under Pure Squeeze Conditions Using Genetic Algorithms

Vibhav Santhanam

A thesis submitted for the degree of Master of Science in Mechanical Engineering

Department of Mechanical Engineering

Kate Gleason College of Engineering

Rochester Institute of Technology, Rochester, NY

2022

Approved Dec 14

Advisor: Dr Stephen Boedo

Committee: Dr Hany Ghoneim, Dr Patricia Iglesias

Department Representative: Dr Sarilyn Ivancic

Contents

List of Figures

List of Tables

Abstract

The purpose of this thesis is to determine the optimal shape of lubricated axisymmetric spherical bearing cups and symmetric journal bearing sleeves under transient pure squeeze conditions using a genetic algorithm. The objective is to maximize the load impulse of a perfectly spherical ball or perfectly cylindrical journal interacting through a thin lubricant film with a generally non-spherical cup or non-cylindrical sleeve to achieve a specified minimum film thickness value. A generation is a set of bearing shapes over the design space encoded as binary chromosomes. A finite element model simulates the normal approach of the ball or journal to the cup or sleeve and the fitness of each shape is measured by load impulse. A new generation is formed by splitting and recombining chromosomes while conserving the top two fittest solutions and applying random mutations to the rest. This process is repeated for a fixed number of generations, after which the fittest design is selected as the "optimal" shape. It was found that optimal shapes produced by the genetic algorithm yielded generally higher impulse values than those obtained with perfectly spherical or cylindrical bearings, but the gain in performance over specified elliptical shapes was mixed over the design space.

Chapter 1

Introduction

1.1 Background

Hydrodynamic self-acting cylindrical (journal) and spherical bearings operate with a thin lubricant film between the interacting surfaces. Pressure is generated within the film from relative transverse surface motion (shear action) and relative normal approach (squeeze action). Lubricant is typically supplied through edge, groove, or feed hole arrangements at substantially low supply pressure by an oil pump or drip/splash methods. If the resulting film pressures can generate a film thickness large enough to minimize surface asperity contact, friction can be substantially reduced.

Hydrodynamic cylindrical bearings are ubiquitous and appear in virtually any machine with rotating parts, with motors, pumps, drivetrains, household appliances, and watches being just a few examples. Hydrodynamic spherical bearings have many applications including artificial joints, automotive suspensions, heavy machinery, and robotic mechanisms.

1.1.1 Literature Review

Traditional Design Guidelines

Traditional design guidelines for cylindrical and spherical bearings usually assume a uniform radial clearance. Examples in the literature for cylindrical bearings under steady load and speed are found in standard textbooks (e.g., Budynas and Nisbett [13]). Design of journal bearings for specialty applications, such as connecting-rod bearings in four-stroke engines are also available in the literature (e.g., Booker [9], Boedo [2], Boedo and Blais [6]).

Work performed by Goenka and Booker [18] provides a foundation for the finite element analysis of spherical bearings. Figure 1.1 shows the bearing geometry. Both explicit (determining bearing force history given specified ball displacement history) and implicit (determining ball displacement history given force history) problems can be solved with this method. In the pure squeeze problem (i.e.,, no rotation and constant load) it was found that the mesh density was not important when eccentricity – the displacement of the ball from the center of the bearing – was small but that it did cause significant difference in results when the eccentricity was large. Partial spherical bearings were simulated with various span angles, and it was found that smaller span angles resulted in a lower pressure ratio ($\frac{\text{pressure}}{\text{applied load}}$). Figure 1.2 shows non-dimensional squeeze film forces for various span angles. Since perfectly spherical geometry was assumed for both full and truncated hemispheres, no conclusions could be drawn from this study on the optimal shape of a spherical bearing cup.

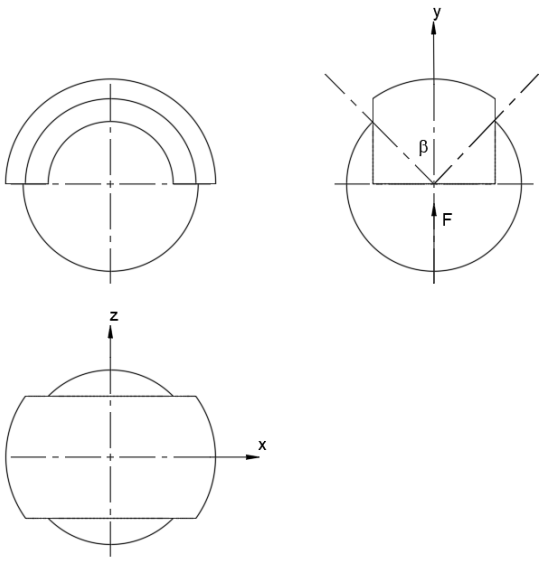

Figure 1.1: Orthographic view of partial spherical bearing with definition of span angle β (based on [18])

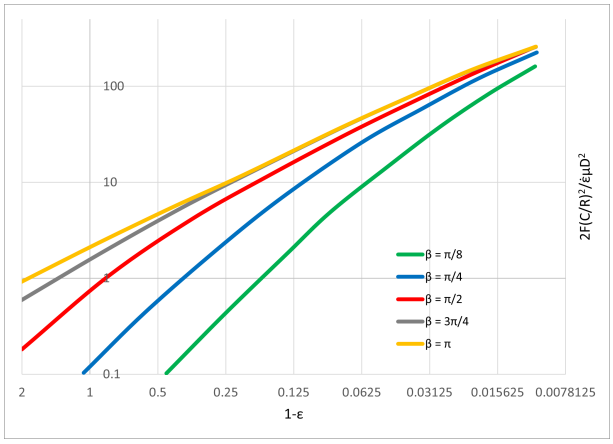

Figure 1.2: Effect of span angle and eccentricity on dimensionless squeeze film force (based on [18])

However, such bearing clerarances are seldom uniform in practice due to manufacturing tolerances or distortion due to thermal expansion. The situation is further complicated by surface deformations due to applied bearing load.

Optimal Journal Bearing Design

For self-acting cylindrical bearings, there have been a significant number of studies on intentional deviation from perfect cylindricity as a means to improve bearing performance.

Wang et al. [37] examined the pressure characteristics, cavitation, and thermal effects of elliptical bearings under steady load and speed and an optimal ellipticity ratio that had the least cavitation, lowest rise in temperature, and the most effective formation of a lubrication film. Hashimoto et al. [21] analyzed steadily loaded elliptical bearings in the turbulent flow regime, with one of the findings being less oil whirl in elliptical bearings compared to circular bearings at a given speed. Vaidyanathan and Keith [34] [33] employed the Elrod algorithm to predict cavitation, pressure, and the rupture and reformation boundaries in various non-circular bearings. Goenka and Booker [19] performed a finite element analysis on elliptical bearing surfaces to determine the optimal shape of the sleeve and journal under oscillatory journal motion and steady load, and found that an elliptical sleeve with a circular journal was best, with a minimum film thickness 36 times that of a regular bearing, and a maximum pressure 5 times lower.

Offset bearings, which have one or more journal and/or sleeve sections that are not concentric with the main one, can improve performance in applications such as 2-stroke diesel engines. In such cases, the journal oscillates within a narrow angular range and the load never reverses, resulting in extremely thin lubricant films and high friction and wear. The offset geometry allows for the load to be shared between the multiple sections and for a thick film lubrication regime to develop as the journal rocks back and forth within the bearing. Studies done by Booker and Olikara [12], Booker et al. [10], Wakuri et al. [35], and Boedo and Anderson [5] show that offset journal bearings have greater film thickness, lower maximum pressure, and improved durability than conventional ones. An improved study by Boedo and Booker [7] using exact numerical methods and mass conserving cavitation analysis supports these results.

The shape optimization of journal bearings without regard to specific geometry has been examined by several authors. Early examples are Maday [25] and Rohde [31] who found that stepped concentric bearings (as shown in Figure 1.4) have an higher load

capacity than purely circular bearings. Kanarachos [24] added dynamic performance characteristics, expressed by the spring and damping constants of the bearing, into the optimization process. Haraldsson et al. [20] optimized the shape of a journal bearing with a rubber layer inside the housing and water as the lubricating fluid, with the objective of minimizing the maximum pressures developed inside.

A basis for shape optimization of bearings using genetic algorithms is provided by Boedo and Eshkabilov [16] who implemented a genetic algorithm (GA) to optimize the shape of a finite-width isoviscous fluid film journal bearing under steady load and steady journal rotation. The objective was to maximize the bearing load capacity, subject to a specified minimum film thickness. The loads were determined with a finite element program using a lubrication algorithm described by Booker and Huebner [11] and 4-noded isoparametric elements. The design variables, defined by film thickness specifications at regularly spaced angular positions about the bearing sleeve circumference, were encoded into a chromosome composed of binary digits. A chromosome's fitness was evaluated by its load capacity. Figure 1.3 shows the optimal shapes of non-cylindrical and cylindrical bearings that maximize load capacity for a specified minimum film thickness of 5 μm. It was found that the shape determined by the GA had a slightly higher load capacity than a perfectly cylindrical bearing, but substantially larger overall film thickness, allowing for better manufacturability and enhanced oil flow. The GA was found to produce better results than a random search in less time. Pang et al. [29] did a similar study, but using a fourier series function instead of individual clearance values, to represent the profile, with the intent of creating a smoother shape. The optimized shape created resulted in a 11.2 percent improvement in the load capacity over that of Boedo and Eshkabilov. Other studies done by Pang et al. [27] [30] [28] use other methods to maximize multiple different performance characteristics of journal bearings. Elsharkawy and Guedouar [15] present a solution to an inverse problem for the elastohydrodynamic lubrication of one-layered journal bearings, where the eccentricity ratio, lubricant viscosity and bulk modulus, and pressure-viscosity coefficient are estimated from a given pressure distribution. Wang et al. [38] present an engineering approach for optimizing the performance of fluid film lubricated

bearings, using a numerical optimization procedure. When elliptical bearings were analyzed, it was revealed that high eccentricity ratio and two large pressure zones for high-speed stability can be obtained by maximizing film pressures in the upper and lower lobes.

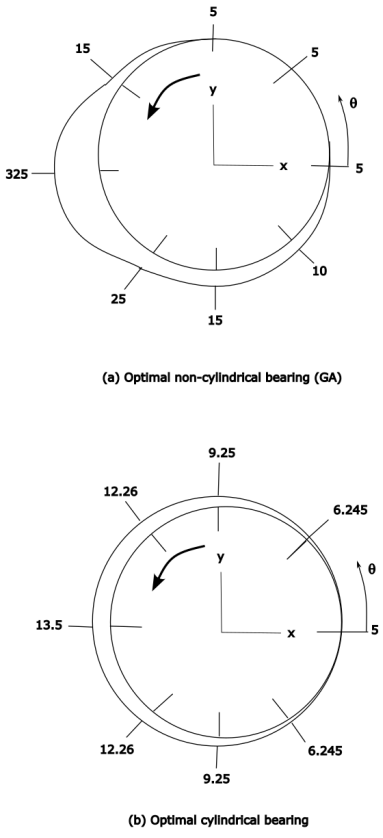

Figure 1.3: Optimal shapes of journal bearings; clearances in μm (based on [16])

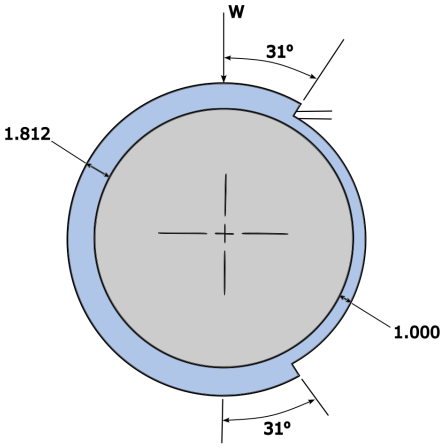

Figure 1.4: Optimal journal bearing shape (based on [25])

Optimal Spherical Bearing Design

Compared to journal bearings, there is much less information in the literature on the lubrication and shape optimization of spherical (or ball and cup) bearings. The study of the effect of non-spherical geometry has been essentially limited to artificial hip joints. Jin and Dowson [23] performed numerical analysis of hydrodyamic lubrication of artificial hip joint replacements with high modulus of elasticity (i.e.„ metal-on-metal, ceramic-on-ceramic) under cyclic walking conditions. It was found that a lubricating film thickness can be developed during the walking cycle due to the combined action of squeeze film and entraining motions, and that a dimple on the acetabular cup can significantly increase the film thickness throughout the walking cycle. A study by Gao et al. [17] found that an "Alpharabola" cup improved the lubricant film thickness and reduced the hydrodynamic pressure of a metal-on-metal hip replacement, but contrary to Jin and Dowson, the dimples had an adverse effect on these characteristics. Another study by Meng et al. [26] examined an Alpharabola ball and spherical cup and found that it was superior to a spherical ball and spherical cup, but inferior to the spherical ball and Alpharabola cup. Wang et al. [36] studied both ellipsoidal balls and cups, and concluded that a "well controlled nonsphericity" was beneficial for improving the lubrication of the

bearing. A study of artificial hip joints by Boedo and Booker [8] provides insights on further geometry modifications of these cups. A finite element analysis was performed of an ellipsoidal cup shown in Figure 1.5, with elastic protrusions extending from the cup surface towards the ball, as well a wide cut-out slot. During the stance phase (the load bearing phase) of the walking cycle, a majority of the load is carried by the lubricant between the cup and the ball due to squeeze film action, while a minority is carried by the elastic elements. These modifications were found to result in a larger minimum film thickness and lower pressures during the stance phase as shown in Figure 1.6, making the modified bearing superior to a spherical bearing as a hip replacement.

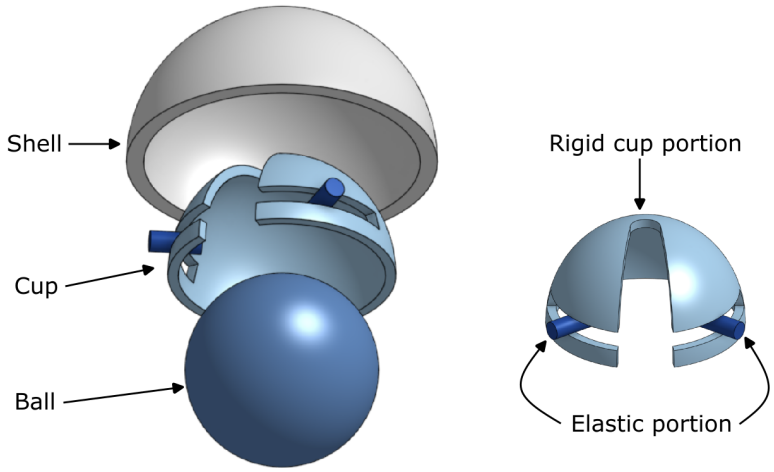

Figure 1.5: Squeeze film artificial hip joint (based on [8])

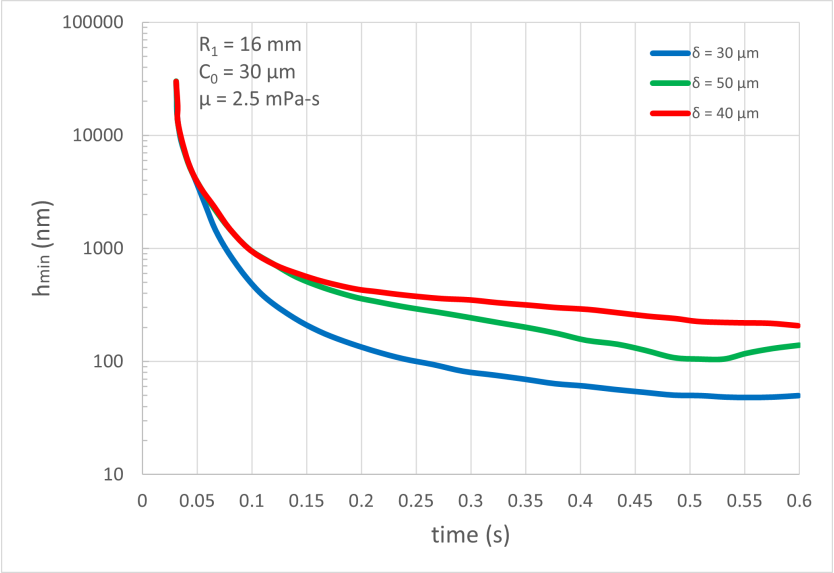

Figure 1.6: Effect of ellipticity on minimum film thickness over time (based on [8])

One self-acting spherical bearing not associated with biomechanical applications is the so-called Hydrosphere [32] shown in Figure 1.7. Under the prescribed axial loading and spherical rotation with perfectly spherical surfaces, the bearing has theoretically zero load capacity, yet a load-supporting hydrodynamic film was experimentally generated. An explanation was later put forth by Dowson and Taylor [14] that thermal effects were sufficient to distort the spherical surfaces and generate a load-carrying wedge film.

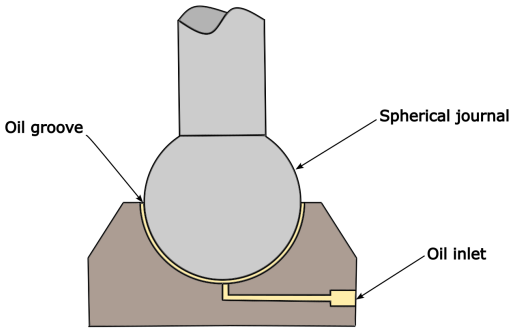

Figure 1.7: Hydrosphere (based on [32])

1.2 Thesis Objective

There are no papers in the literature which address general shape optimization of bearing surfaces under transient loads and kinematics. This thesis concerns the shape optimization of axisymmetric spherical and cylindrical squeeze-film bearings under transient pure squeeze conditions using genetic algorithms (GA).

Figure 1.8 shows an example of a spherical bearing system – an artificial hip joint. The joint is composed of the femoral head (ball), which is made out of ceramic or a hard metal; a polyethylene liner; and a metal shell. In this specific case, the optimal shape determined in this thesis would be applied to the polyethylene liner.

Figure 1.9 shows an example of a journal bearing system consisting of a cylindrical journal (in this case, composed of several tilting pads) and a sleeve with a circular profile. All parts in this example are made of metal, but there are a variety of different materials that can be used for the bushing (the part of the bearing that directly interfaces with the journal), including plastic, ceramic, and even jewels.

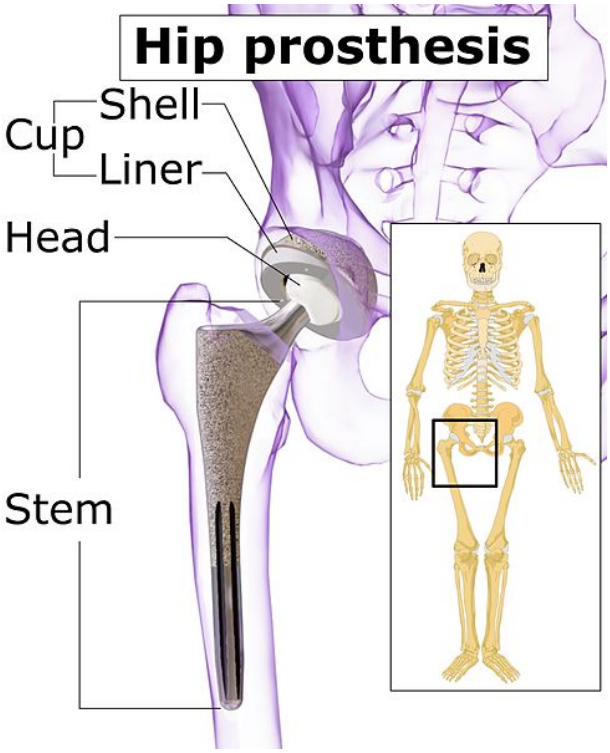

Figure 1.8: Spherical bearing example [22]

Figure 1.9: Cylindrical bearing example [1]

The objective of this thesis is to determine the bearing cup shape (for spherical bearings) and the bearing sleeve shape (for cylindrical bearings) that maximizes the total impulse, defined by the load multiplied by the time required to reach a specified minimum film thickness h^*_{min}. The problem only concerns the normal approach of the ball/journal to the cup/sleeve absent of ball/journal rotation, in contrast to previous work done in bearing shape optimization which involved journal bearings under constant rotation.

The methodology required to accomplish this task are the following:

- Create a finite element program that allows for variation in the geometry of the bearing cup or sleeve in the simulation of the pure squeeze scenario involving the cup and a spherical ball, or a sleeve and a cylindrical journal, respectively, where the resolution of the design space is independent of the resolution of the finite element mesh.

- Implement a genetic algorithm to determine optimal shape through solution convergence. As in Boedo and Eshkabilov [16], elitism, crossover, and mutation operators are used.

- Using the modified finite element program, simulate the natural selection process with the genetic algorithm starting with a set of randomly generated designs for a fixed number of generations that is likely to result in improvement of bearing load capacity.

Chapter 2

Problem Formulation

2.1 Spherical Bearing

2.1.1 Description of Design Space

Figure 2.1 shows a spherical ball and a generally non-spherical but axisymmetric (about the Z axis) cup separated by a thin layer of lubricant with viscosity μ. The ball and cup are initially concentric, and the bearing film is initially complete. A constant normal external load F is applied to the ball, which causes the ball to move toward the cup and the fluid to squeeze out of the bearing. The squeeze film action provides a damping force to the ball, and the ball will approach the cup asymptotically in the limit as t $\rightarrow \infty$.

The radial clearance between the ball and the cup is defined when the ball and cup are concentric. The radial clearance is allowed to vary from a nominal value C_0 at equally spaced points along the circumference of the cup. Figure 2.2 shows the design space consisting of N points, spaced equally at an angle of α $(\alpha = \frac{\theta_0}{N})$ with specified non-negative radial clearance deviations δ_1 through δ_N. The radial clearance at node N+1 is set to C_0 $(\delta_{N+1} = 0)$ at the edge (extent) of the cup, i.e.,, at $\theta = \theta_0$, and is not a design variable.

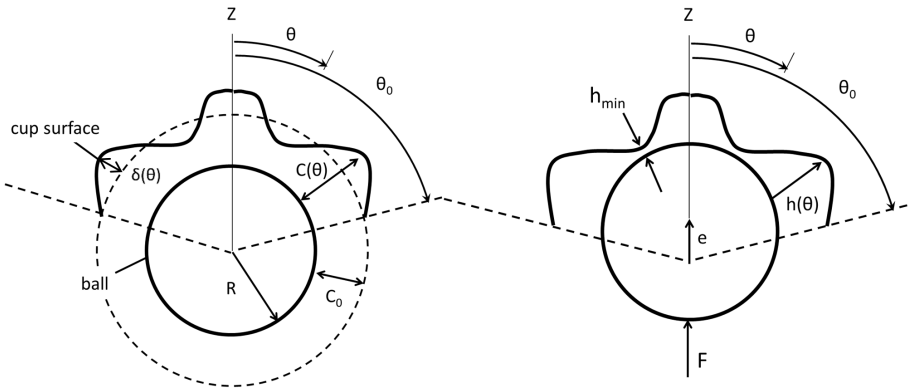

Figure 2.1: Spherical bearing schematic

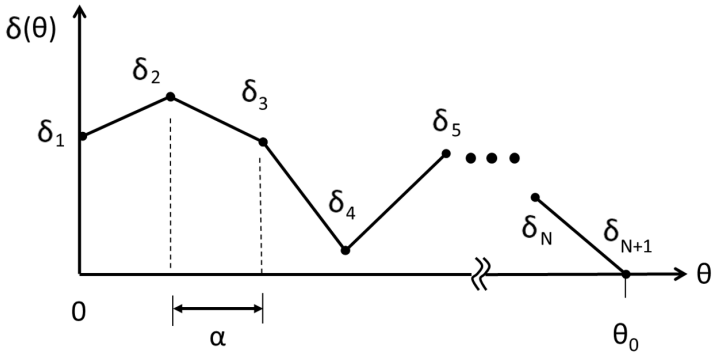

Figure 2.2: Radial clearance specification

The radial clearance deviation, as a function of θ, is assumed to vary linearly, given by

$$\delta(\theta) = \delta_i + \frac{(\delta_{i+1} - \delta_i)}{\alpha}[\theta - (i-1)\alpha] \tag{2.1}$$

where $(i-1)\alpha \leq \theta \leq i\alpha$ and $0 \leq \delta_i \leq \delta_{max}$, $i = 1, N$ (δ_{max} is the maximum allowable clearance).

The film thickness $h(\theta)$ defined in Figure 2.1 is in turn given by

$$h(\theta) = C_0 + \delta(\theta) - e\cos\theta \tag{2.2}$$

which is also dependent on the ball displacement (eccentricity) e.

Figure 2.3 shows the lubricant film domain projected onto a 2D view. Here the x and θ axes run from the center of the bearing to the edge. The location of the edge of the bearing cup depends on θ_0, the angular extent of the cup, but the projected shape remains the same (circular).

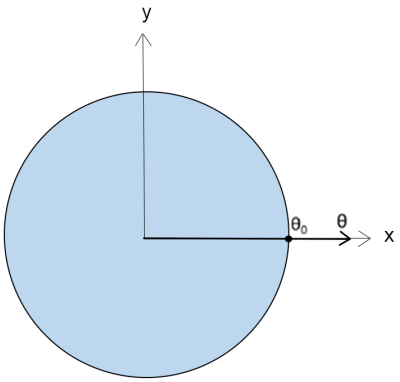

Figure 2.3: Lubricant film domain (2 dimensional)

2.1.2 Force and Impulse

The Reynolds equation in axisymmetric form is given by [18]

$$\frac{\partial}{\partial\theta}\left(\frac{h^3}{12\mu}\sin\theta\frac{\partial p}{\partial\theta}\right) = -R^2\dot{e}\sin\theta\cos\theta \tag{2.3}$$

where

$$h(\theta) = f(\theta;\theta_0, C_0, \delta_0, \delta_1, \delta_2, ..., \delta_N) - e\cos\theta \tag{2.4}$$

with boundary conditions

$$p(\theta = \theta_0) = 0 \quad \text{and} \quad \frac{dp}{d\theta}(\theta = 0) = 0 \tag{2.5}$$

The load F carried by the lubricant film is given by

$$F = 2\pi R^2 \int_0^{\theta_0} p \cos\theta \sin\theta d\theta \tag{2.6}$$

and the impulse I after a given time interval T is given by

$$I = \int_0^T F dt = FT \tag{2.7}$$

The ball and cup are initially concentric, i.e.,, $e(t = 0) = 0$.

2.1.3 Squeeze Film Problem (Dimensional)

With ball and cup initially concentric, a constant external force F is applied to the ball along the symmetry axis. Given the bearing geometry, fluid viscosity, radial clearance design space, and the target minimum film thickness h^*_{min}, the time history of journal eccentricity e(t) is obtained from solution of equations 2.3 – 2.6. The simulation is run until time T^* when h^*_{min} is attained, which in turn gives the resultant impulse $I = \int_0^{T^*} F dt = FT^*$

In dimensional terms, given maximum allowable clearance deviation δ_{max} and target minimum film thickness h^*_{min}, the optimization problem is to find the set of radial clearances $\delta_1, \delta_2, ..., \delta_N, 0 \leq \delta_i \leq \delta_{max}$, that maximizes impulse I.

2.1.4 Non-dimensionalization

To make the solution valid at any dimensional scale, the problem will be expressed and solved non-dimensionally, with the aim of maximizing the non-dimensional impulse as shown below.

Film thickness, eccentricity, and radial clearance deviation are all scaled by reference (edge) radial clearance C_0, namely,

$$h = C_0 \bar{h}$$
$$e = C_0 \epsilon$$
$$\delta_i = C_0 \bar{\delta}_i \qquad i = 1, N$$

where non-dimensional film thickness has the functional form

$$\bar{h}(\theta) = f(\theta; \theta_0, \bar{\delta}_1, \bar{\delta}_2, ..., \bar{\delta}_N) - \epsilon \cos\theta \tag{2.8}$$

with ball eccentricity ratio ϵ. Plugging these into equation 2.3 gives

$$\frac{\partial}{\partial\theta}(\bar{h}^3 \sin\theta \frac{\partial p}{\partial\theta}) = -12\mu(\frac{R}{C_0})^2 \dot{\epsilon} \sin\theta\cos\theta \tag{2.9}$$

Defining the non-dimensional pressure according to $p = \mu(\frac{R}{C_0})^2 \dot{\epsilon}\bar{p}$, we can express the Reynolds equation in non-dimensional form as

$$\frac{\partial}{\partial\theta}(\bar{h}^3 \sin\theta \frac{\partial \bar{p}}{\partial\theta}) = -12 \sin\theta\cos\theta \tag{2.10}$$

with boundary conditions

$$\bar{p}(\theta = \theta_0) = 0 \quad \text{and} \quad \frac{d\bar{p}}{d\theta}(\theta = 0) = 0 \tag{2.11}$$

The load, expressed as an integral of the non-dimensional pressure, is

$$F = 2\pi R^2 \mu(\frac{R}{C_0})^2 \dot{\epsilon} \int_0^{\theta_0} \bar{p} \cos\theta \sin\theta d\theta \tag{2.12}$$

Multiplying by dt gives

$$Fdt = 2\pi R^2 \mu(\frac{R}{C_0})^2 d\epsilon \int_0^{\theta_0} \bar{p} \cos\theta \sin\theta d\theta \tag{2.13}$$

Integrating with respect to time from 0 to T^* gives the impulse

$$I = \int_0^{\epsilon_{T^*}} 2\pi R^2 \mu (\frac{R}{C_0})^2 [\int_0^{\theta_0} \bar{p} \cos\theta \sin\theta d\theta] d\epsilon \tag{2.14}$$

where ϵ_{T^*} is the ball eccentricity ratio at time T^*, where $\frac{h^*_{min}}{C_0}$ is specified. Rearranging we obtain the non-dimensional impulse

$$\frac{I(\frac{C_0}{R})^2}{\pi R^2 \mu} = 2 \int_0^{\epsilon_{T^*}} \int_0^{\theta_0} \bar{p} \cos\theta \sin\theta d\theta d\epsilon \tag{2.15}$$

2.1.5 Squeeze Film Problem (Non-Dimensional)

Given the radial clearance deviation design space defined by
$\bar{\delta}_1, \bar{\delta}_2, ..., \bar{\delta}_N, \bar{\delta}_{max}$; $\bar{\delta}_{N+1} = 0$; $0 < \bar{\delta}_i \leq \bar{\delta}_{max}$; and given $\frac{h^*_{min}}{C_0}$, the target non-dimensional film thickness, find ball position ϵ_{T^*} corresponding to $\frac{h^*_{min}}{C_0}$, and find the resultant non-dimensional impulse $\frac{I(\frac{C_0}{R})^2}{\pi R^2 \mu}$ from simultaneous solution of equations 2.8 – 2.15.

In non-dimensional terms, given maximum allowable clearance deviation $\bar{\delta}_{max}$ and target minimum film thickness $\frac{h^*_{min}}{C_0}$, the optimization problem is to find the
$\bar{\delta}_1, \bar{\delta}_2, ..., \bar{\delta}_N$; $0 \leq \bar{\delta}_i \leq \bar{\delta}_{max}$; $\bar{\delta}_{N+1} = 0$ such that the non-dimensional impulse $\frac{I(\frac{C_0}{R})^2}{\pi R^2 \mu}$ is a maximum.

2.2 Cylindrical Bearing

2.2.1 Description of Design Space

Figure 2.4 shows a cylindrical journal and a generally non-cylindricial but symmetric (about the XZ plane) sleeve separated by a thin layer of lubricant with viscosity μ. The radial clearance between the journal and the sleeve is defined when the journal and sleeve are concentric. The radial clearance is allowed to vary from a nominal value C_0 at equally spaced points along the circumference of the sleeve. The journal and sleeve are initially concentric, and the bearing film is initially complete. A constant normal external load F is applied to the journal, which causes the journal to move toward the sleeve and the fluid to

squeeze out of the bearing. The squeeze film action provides a damping force to the journal, and the journal will approach the sleeve asymptotically in the limit as t $\rightarrow \infty$.

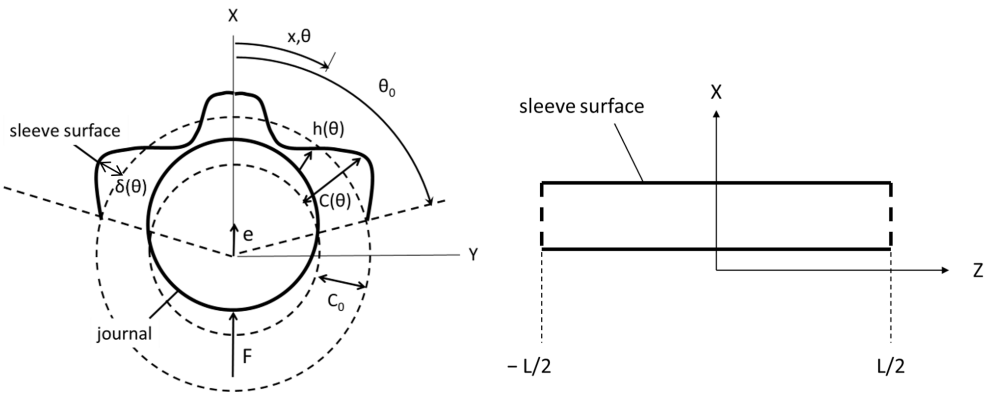

Figure 2.4: Cylindrical bearing schematic

Figure 2.5 shows the lubricant film domain "unwrapped" and flattened into a 2D view. Here the x axis runs along what would be the circumference of the bearing and the y axis is parallel to the original Z axis.

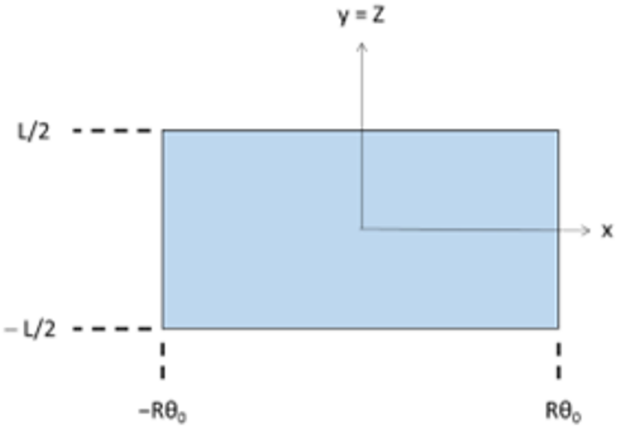

Figure 2.5: Lubricant film domain (2 dimensional)

As in the spherical bearing, the design space consists of N points, spaced equally at an angle of $\alpha \quad (\alpha = \frac{\theta_0}{N})$ with specified non-negative radial clearance deviations δ_1 through δ_N. The radial clearance at node N+1 is set to $C_0 \quad (\delta_{N+1} = 0)$ at the edge (extent) of the sleeve, i.e.,, at $\theta = \theta_0$, and is not a design variable.

2.2.2 Generalized Warner Bearing Film Model

The following is taken directly from Boedo [4] and is provided here for completeness. Assume that film pressure can be represented in the separable form

$$p(\theta, y, t) = g(\theta, t) f(y) \tag{2.16}$$

where $g(\theta, t)$ is the circumferential pressure distribution along the bearing midplane, and $f(y)$ is a *prescribed* axial profile with the requirement that $f(y = 0) = 1, \quad f(y = \pm\frac{L}{2}) = 0$.

A prescribed axial profile motivated by the work of Warner [39] takes the functional form

$$f(y) = \frac{\cosh(\frac{\lambda L}{D}) - \cosh[(\frac{2y}{L})(\frac{\lambda L}{D})]}{\cosh(\frac{\lambda L}{d}) - 1} \tag{2.17}$$

which is dependent upon *both* $\frac{L}{D}$ ratio and a prescribed shape factor λ, and plotted in Figure 2.6.

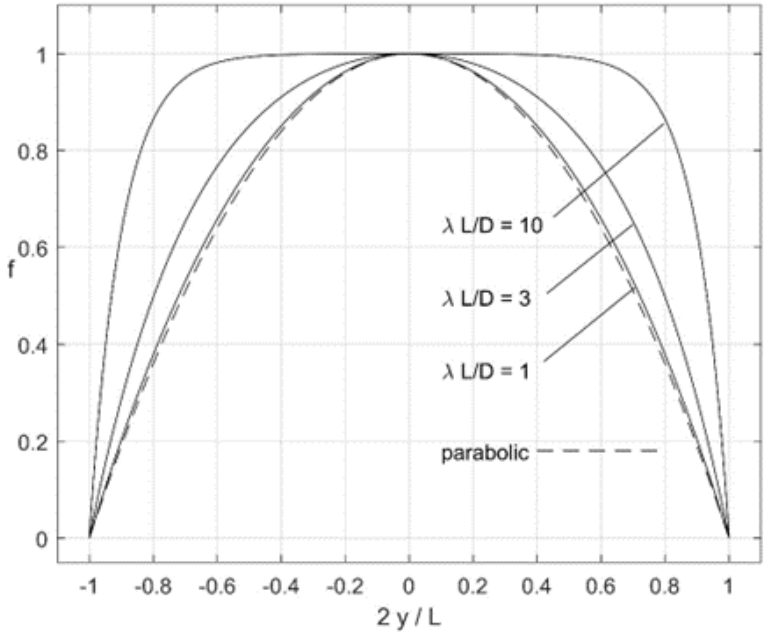

Figure 2.6: Prescribed axial profile $f(y)$ [4]

Note that $f(y)$ approaches parabolic and uniform axial profiles as $\frac{\lambda L}{D} \to 0$ and $\frac{\lambda L}{D} \to \infty$, respectively.

By allowing the shape factor λ to vary with film thickness, $f(y)$ can capture the local flattening of the axial profile expected with very thin films in journal bearings, even with small $\frac{L}{D}$ ratios. One means of accomplishing this task is to assume that λ takes the local form

$$\lambda^2(s) = \frac{24s^2H}{(1-s^2)[12H - 8s(3+s^2) - 3\pi(2-3s^2)]} \tag{2.18}$$

in terms of a local eccentricity ratio

$$s = 1 - \frac{h(\theta)}{C(\theta)} \tag{2.19}$$

with

$$H = s + \frac{\cos^{-1}(-s)}{(1-s^2)^{1/2}} \tag{2.20}$$

and is plotted in Figure 2.7.

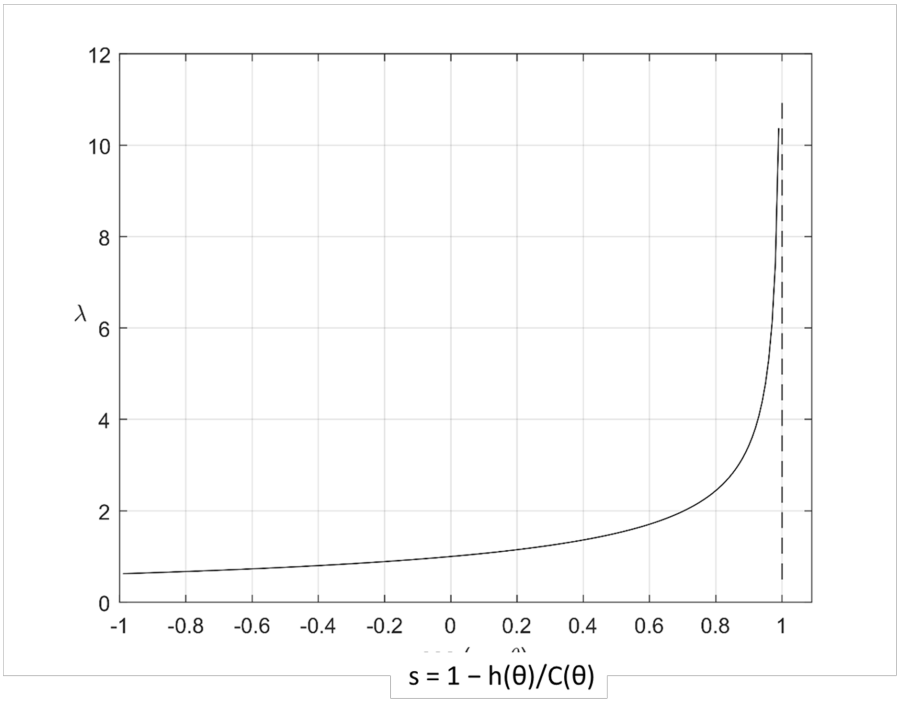

Figure 2.7: λ as it varies with non-dimensional eccentricity ratio s [4]

The assumed form of the pressure distribution minimizes the modified power functional [3, 4] provided that the midplane pressure $g(\theta, t)$ satisfies the Euler-Lagrange equation

$$\frac{1}{R^2}\frac{\partial}{\partial\theta}\left(\frac{h^3\Gamma_1}{12\mu}\frac{\partial g}{\partial\theta}\right) - \Gamma_2\frac{h^3 g}{12L^2\mu} = -\Gamma_3\dot{e}\cos\theta \tag{2.21}$$

with boundary conditions

$$g(\theta = \theta_0, t) = 0$$
$$\frac{dg}{d\theta}(\theta = 0, t) = 0$$

Functions Γ_1, Γ_2, and Γ_3 are designated as flow factors which take the local form

$$\Gamma_1(\gamma) = \frac{\gamma\cosh\gamma - \sinh\gamma}{\gamma(\cosh\gamma - 1)}$$
$$\Gamma_2(\gamma) = \frac{4\gamma(\sinh 2\gamma - 2\gamma)(\gamma\cosh\gamma - \sinh\gamma)}{(\cosh\gamma - 1)[2\gamma(\cosh 2\gamma + 2) - 3\sinh 2\gamma)]}$$
$$\Gamma_3(\gamma) = \frac{4(\gamma\cosh\gamma - \sinh\gamma)^2}{\gamma[2\gamma(\cosh 2\gamma + 2) - 3\sinh 2\gamma)]}$$

where $\gamma = \lambda\frac{L}{D}$.

The load F carried by the lubricant film is given by

$$F = 2\pi R^2 \int_{-L/2}^{L/2} f(y)g(\theta,t)\cos\theta d\theta dy \tag{2.22}$$

and the impulse I after a given time interval T is given by

$$I = \int_0^T F dt = FT \tag{2.23}$$

The journal and sleeve are initially concentric, i.e., $e(t=0) = 0$.

2.2.3 Squeeze Film Problem (Dimensional)

With journal and sleeve initially concentric, a constant external force F is applied to the journal along the symmetry axis. Given the bearing geometry, fluid viscosity, radial clearance design space, the target minimum film thickness h^*_{min}, and $\frac{L}{D}$ ratio, the time history of journal eccentricity e(t) is obtained from solution of equations 2.21 – 2.22. The simulation is run until time T^* when h^*_{min} is attained, which in turn gives the resultant impulse $I = \int_0^{T^*} F dt = FT^*$

In dimensional terms, given maximum allowable clearance deviation δ_{max} and target minimum film thickness h^*_{min}, the optimization problem is to find the set of radial clearance deviations $\delta_1, \delta_2, ..., \delta_N, 0 \leq \delta_i \leq \delta_{max}$, that maximizes impulse I.

2.2.4 Non-dimensionalization

To make the solution valid at any dimensional scale, the problem will be expressed and solved non-dimensionally, with the aim of maximizing the non-dimensional impulse as shown below.

Film thickness, eccentricity, and radial clearance deviation are all scaled by reference (edge) radial clearance C_0, namely,

$$h = C_0\bar{h}$$
$$e = C_0\epsilon$$
$$\delta_i = C_0\bar{\delta}_i \qquad i = 1, N$$

where non-dimensional film thickness has the functional form

$$\bar{h}(\theta) = f(\theta; \theta_0, \bar{\delta}_1, \bar{\delta}_2, ..., \bar{\delta}_N) - \epsilon\cos\theta \tag{2.24}$$

with journal eccentricity ratio ϵ.
Plugging these into equation 2.21 gives

$$\frac{(C_0/R)^2}{\mu}\frac{\partial}{\partial\theta}(\frac{\bar{h}^3\Gamma_1}{12}\frac{\partial g}{\partial\theta}) - \Gamma_2(\frac{D}{L})^2\frac{(C_0/R)^2}{\mu}\frac{\bar{h}^3 g}{48} = -\Gamma_3\dot{\epsilon}\cos\theta \tag{2.25}$$

where flow factors Γ_1, Γ_2, and Γ_3 already depend on ϵ, $\frac{L}{D}$, and the clearance ratio terms.

Defining the non-dimensional circumferential pressure distribution along the bearing midplane according to $g = \mu(\frac{R}{C_0})^2\dot{\epsilon}\bar{g}$, we can express the Euler-Lagrange equation in non-dimensional form as

$$\frac{\partial}{\partial\theta}(\frac{\bar{h}^3\Gamma_1}{12}\frac{\partial\bar{g}}{\partial\theta}) - \Gamma_2(\frac{D}{L})^2\frac{\bar{h}^3\bar{g}}{48} = -\Gamma_3\cos\theta \tag{2.26}$$

with boundary conditions

$$\bar{g}(\theta = \theta_0) = 0 \quad \text{and} \quad \frac{d\bar{g}}{d\theta}(\theta = 0) = 0 \tag{2.27}$$

The load, expressed as an integral of the non-dimensional pressure, is

$$F = \mu(\frac{R}{C_0})^2 \dot{\epsilon} LR \int_{-1}^{1} \int_{0}^{\theta_0} f(\bar{y})\bar{g} \cos\theta d\theta d\bar{y} \tag{2.28}$$

where the non-dimensional displacement along the y-axis of the 2D film domain is defined according to $y = \frac{L\bar{y}}{2}$.
Multiplying by dt and replacing radius with diameter gives

$$Fdt = \mu(\frac{R}{C_0})^2 LD[\frac{1}{2} \int_{-1}^{1} \int_{0}^{\theta_0} f(\bar{y})\bar{g} \cos\theta d\theta d\bar{y}]d\epsilon \tag{2.29}$$

Integrating with respect to time from 0 to T^* gives the impulse

$$I = \int_{0}^{\epsilon_{T^*}} \mu(\frac{R}{C_0})^2 LD[\frac{1}{2} \int_{-1}^{1} \int_{0}^{\theta_0} f(\bar{y})\bar{g} \cos\theta d\theta d\bar{y}]d\epsilon \tag{2.30}$$

where ϵ_{T^*} is the journal eccentricity ratio at time T^*, where $\frac{h^*_{min}}{C_0}$ is specified.
Rearranging we obtain the non-dimensional impulse

$$\frac{I(\frac{C_0}{R})^2}{\mu LD} = \frac{1}{2} \int_{0}^{\epsilon_{T^*}} \int_{-1}^{1} \int_{0}^{\theta_0} f(\bar{y})\bar{g} \cos\theta d\theta d\bar{y} d\epsilon \tag{2.31}$$

2.2.5 Squeeze Film Problem (Non-Dimensional)

Given the radial clearance deviation design space defined by
$\bar{\delta}_1, \bar{\delta}_2, ..., \bar{\delta}_N, \bar{\delta}_{max}$; $\bar{\delta}_{N+1} = 0$; $0 < \bar{\delta}_i \leq \bar{\delta}_{max}$; and given $\frac{h^*_{min}}{C_0}$, the target non-dimensional film thickness, and $\frac{L}{D}$ ratio, find ball position ϵ_{T^*} corresponding to $\frac{h^*_{min}}{C_0}$, and find the resultant non-dimensional impulse $\frac{I(\frac{C_0}{R})^2}{LD\mu}$ from simultaneous solution of equations 2.24 – 2.31.

In non-dimensional terms, given maximum allowable clearance deviation $\bar{\delta}_{max}$, target minimum film thickness $\frac{h^*_{min}}{C_0}$, and $\frac{L}{D}$ ratio, the optimization problem is to find the $\bar{\delta}_1, \bar{\delta}_2, ..., \bar{\delta}_N$; $0 \leq \bar{\delta}_i \leq \bar{\delta}_{max}$; $\bar{\delta}_{N+1} = 0$ such that the non-dimensional impulse $\frac{I(\frac{C_0}{R})^2}{LD\mu}$ is a maximum.

2.3 System Formulation

Figure 2.8 shows the one-dimensional finite element mesh of the spherical and cylindrical bearing film domains. Figure 2.9 shows two-dimensional views of the film domains with the finite element mesh overlaid. Figure 2.10 is a diagram of an arbitrary pressure distribution along the one-dimensional mesh.

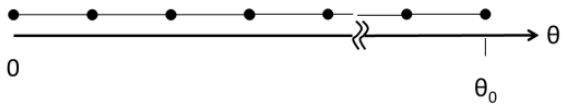

Figure 2.8: Finite element mesh

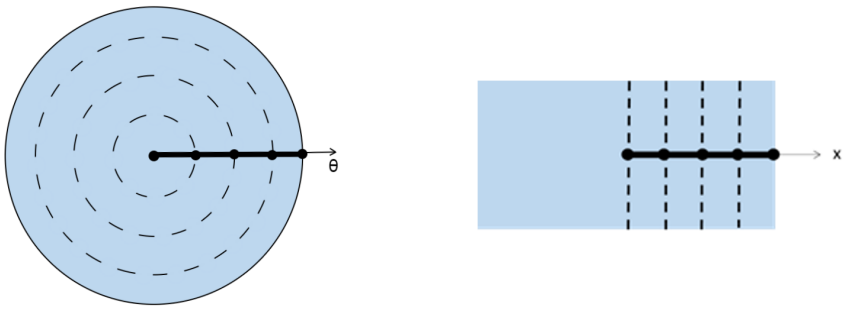

Figure 2.9: Finite element mesh for spherical bearing (L) and cylindrical bearing (R) (2 dimensional view)

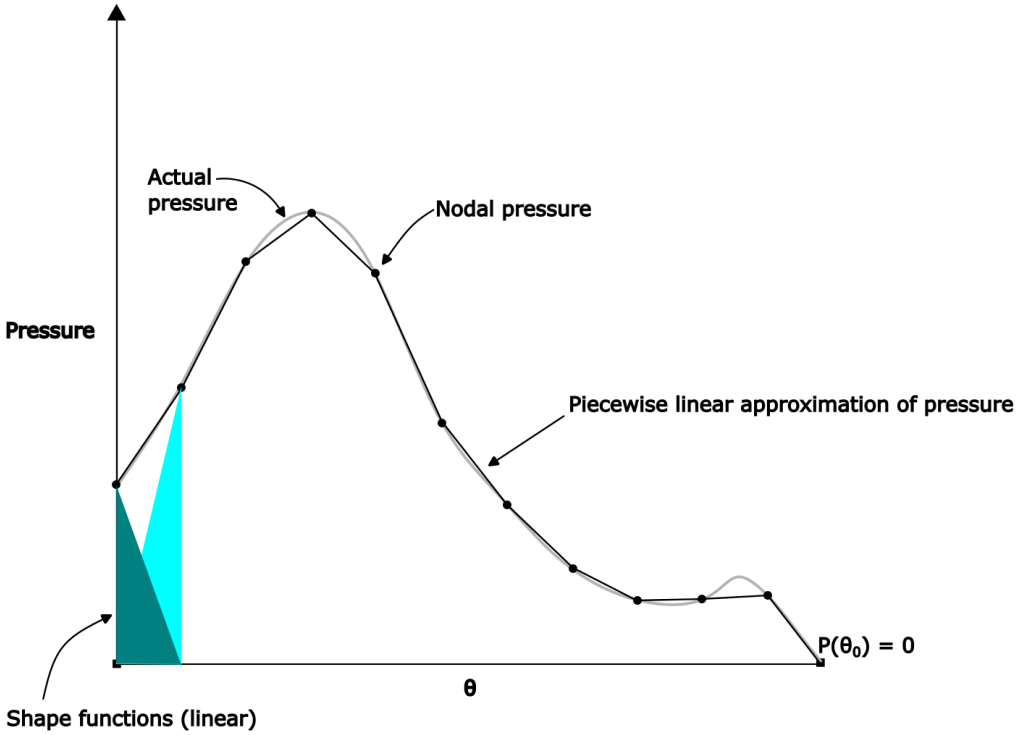

Figure 2.10: Depiction of actual pressure and finite element approximation of pressure

Define the following system variables:

n		number of finite element nodes ($\gg$N)
e	1x1	journal eccentricity along z axis (sphere) and x axis (cylinder) (scalar)
F	1x1	z-component (ball to cup) or x-component (journal to sleeve) of external force (scalar)
$\mathbf{q}$	nx1	nodal net flow
$\mathbf{p}$	nx1	nodal film pressure
$\mathbf{C}$	nx1	nodal radial clearance
$\mathbf{h}$	nx1	nodal film thickness
$\mathbf{r}$	nx1	nodal film forces (film to cup or journal)
$\mathbf{S}$	nx1	squeeze-related matrix
$\mathbf{T}$	1xn	area-related matrix
$\mathbf{G}$	nx1	static equilibrium matrix
$\mathbf{K^p}$	nxn	pressure fluidity matrix
$\mathbf{K^{\dot{h}}}$	nxn	squeeze fluidity matrix
$\mathbf{A}$	nxn	area matrix

(2.32)

At a given instant, film thickness and rate of change are given by

$$\begin{aligned} \mathbf{h} &= \mathbf{C} + \mathrm{e}\mathbf{G} \\ \dot{\mathbf{h}} &= \dot{\mathrm{e}}\mathbf{G} \end{aligned}$$

$$\text{where} \quad \mathbf{G} = \begin{Bmatrix} -\cos\theta_1 \\ \dots \\ -\cos\theta_n \end{Bmatrix} \tag{2.33}$$

Flow-pressure relation is given by

$$\begin{aligned}\mathbf{q} &= \mathbf{K}^{\mathrm{p}}\mathbf{p} + \mathbf{K}^{\dot{\mathrm{h}}}\dot{\mathbf{h}} \\ \mathbf{q} &= \mathbf{K}^{\mathrm{p}}\mathbf{p} + \dot{\mathrm{e}}\mathbf{K}^{\dot{\mathrm{h}}}\mathbf{G} \\ \mathbf{q} &= \mathbf{K}^{\mathrm{p}}\mathbf{p} + \dot{\mathrm{e}}\mathbf{S}\end{aligned} \tag{2.34}$$

Pressure-force relation is given by

$$\mathbf{r} = \mathbf{A}\mathbf{p}$$

and force balance is given by

$$-\mathbf{G}^{\mathrm{T}}\mathbf{r} = \mathrm{F} \tag{2.35}$$

whereupon

$$\begin{aligned}-\mathbf{G}^{\mathrm{T}}\mathbf{A}\mathbf{p} &= \mathrm{F} \\ \mathbf{T}\mathbf{p} &= \mathrm{F}\end{aligned}$$

Partition nodes into two sets:

1 = specified nodal net flow $\mathbf{q_1}$

2 = specified nodal pressure $\mathbf{p_2}$

Equations 2.34 and 2.35 in partitioned form become

$$\begin{aligned}\mathbf{q}_1 &= \mathbf{K}^{\mathrm{p}}_{11}\mathbf{p}_1 + \mathbf{K}^{\mathrm{p}}_{12}\mathbf{p}_2 + \dot{e}\mathbf{S}_1 \\ \mathbf{q}_2 &= \mathbf{K}^{\mathrm{p}}_{21}\mathbf{p}_1 + \mathbf{K}^{\mathrm{p}}_{22}\mathbf{p}_2 + \dot{e}\mathbf{S}_2 \\ \mathbf{T}_1\mathbf{p}_1 &+ \mathbf{T}_2\mathbf{p}_2 = \mathrm{F}\end{aligned} \tag{2.36}$$

The (instantaneous) ball or journal velocity (scalar) is then obtained from

$$\begin{aligned}\mathbf{p}_1 &= (\mathbf{K}^{\mathrm{p}}_{11})^{-1}(\mathbf{q}_1 - \mathbf{K}^{\mathrm{p}}_{12}\mathbf{p}_2 - \dot{\mathrm{e}}\mathbf{S}_1) \\ \mathbf{T}_1(\mathbf{K}^{\mathrm{p}}_{11})^{-1}&(\mathbf{q}_1 - \mathbf{K}^{\mathrm{p}}_{12}\mathbf{p}_2 - \dot{\mathrm{e}}\mathbf{S}_1) + \mathbf{T}_2\mathbf{p}_2 = \mathrm{F} \\ \mathbf{T}_1(\mathbf{K}^{\mathrm{p}}_{11})^{-1}&(\mathbf{q}_1 - \mathbf{K}^{\mathrm{p}}_{12}\mathbf{p}_2) + \mathbf{T}_2\mathbf{p}_2 - \mathrm{F} = \dot{\mathrm{e}}\mathbf{T}_1(\mathbf{K}^{\mathrm{p}}_{11})^{-1}\mathbf{S}_1 \\ \dot{\mathrm{e}} &= [\mathbf{T}_1(\mathbf{K}^{\mathrm{p}}_{11})^{-1}\mathbf{S}_1]^{-1}[\mathbf{T}_1(\mathbf{K}^{\mathrm{p}}_{11})^{-1}(\mathbf{q}_1 - \mathbf{K}^{\mathrm{p}}_{12}\mathbf{p}_2) + \mathbf{T}_2\mathbf{p}_2 - \mathrm{F}]\end{aligned} \tag{2.37}$$

Once that $\dot{\mathbf{e}}$ is obtained, one can then solve for (instantaneous) unknown nodal pressures and flows

$$\begin{aligned} \mathbf{p}_1 &= (\mathbf{K}^{\mathrm{p}}_{11})^{-1}(\mathbf{q}_1 - \mathbf{K}^{\mathrm{p}}_{12}\mathbf{p}_2 - \dot{\mathrm{e}}\mathbf{S}_1) \\ \mathbf{q}_2 &= \mathbf{K}^{\mathrm{p}}_{21}\mathbf{p}_1 + \mathbf{K}^{\mathrm{p}}_{22}\mathbf{p}_2 + \dot{\mathrm{e}}\mathbf{S}_2 \end{aligned} \tag{2.38}$$

2.4 Method

2.4.1 Genetic Algorithm

Following Boedo and Eshkabilov [16], a genetic algorithm (GA) was written with the clearance deviation design variables encoded in binary. The minimum value that the clearance deviation can take on is 0, while the maximum value is $\bar{\delta}_{max} = \lambda(2^M - 1)$, where M is the number of binary digits (bits) used to encode each variable. λ is the resolution, which is the smallest amount that the non-dimensional value of the deviation can be incremented by. For example, if M is 7, there are $2^7 = 128$ values that the non-dimensional radial clearance can take on, from 0 to 127. Figure 2.11 provides an illustration of a single design variable, which is a snippet of a chromosome, consisting of M bits.

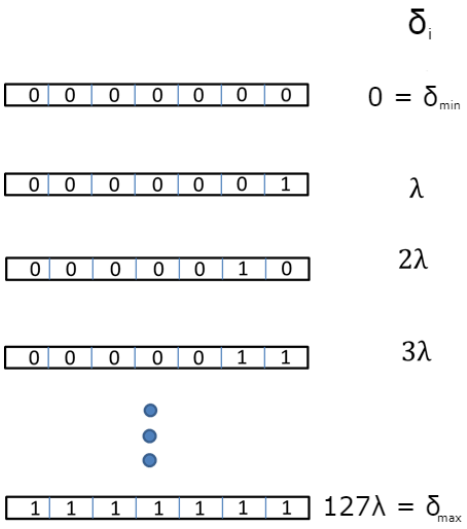

Figure 2.11: Illustration of design variable with values ranging from 0 (top) to 127λ (bottom), which is δ_{max}.

All GAs simulate the process of evolution through natural selection by generating a set of solutions to a function, evaluating their fitness according to some criteria, and selecting and crossing ("breeding") the solutions using a method chosen by the writer of the algorithm. In this case, the solutions are the designs (i.e., the shapes of the bearing cups), which are encoded into binary chromosomes and comprise all the individual variables in the design space. The fitness is the impulse generated by the interaction between the bearing cup and the ball in the squeezing process, with a higher impulse, i.e., a longer time to reach the minimum film thickness given a certain load, being more desirable. The chromosomes are ranked by their impulse, and the top two solutions are carried over to the next generation (known as "elitism"). The remaining chromosomes are cut at random points, and crossed over with other chromosomes to create new chromosomes for the next generation ("crossover"). In addition, mutations in the form of flipping the binary digit (0 to 1 or 1 to 0) are introduced at random points ("mutation"). The algorithm is run for this new set of chromosomes, the chromosomes ranked in order of fitness, and the elitism, crossover, and mutation operators were applied. This process is repeated a number of times set beforehand (number of generations).

The random number generator in Matlab is used to create the original set of chromosomes. Since the random number, n, ranges from $0 \leq n < 1$, the number must be scaled to create the actual design space variable. For the purpose of this thesis, the maximum design space variables were, for the two runs: 1) equal to the initial clearance C_0 ($\bar{\delta}_{max} = 1$), and 2) three times C_0 ($\bar{\delta}_{max} = 3$). These were chosen arbitrarily, but were meant to represent realistic scenarios from a manufacturing perspective.

Several parameters needed to be set before the program was run: P_{cross}, the probability that a chromosome would be cut at a given point; P_{mutat}, the probability that a given digit would be mutated (i.e., flipped from 0 to 1 or 1 to 0); n_{chrom}, the number of chromosomes; n_{var}, the number of design variables in each chromosome; n_{bits} the number of bits in each variable; n_{gen}, the number of generations that the program would be run for. The probabilities, P_{cross} and P_{mutat}, were carried over from the GA developed by Boedo and Eshkabilov for the rotating cylindrical bearing. For this thesis, n_{var} and n_{bits} were set to 10 and 7, respectively. Initially, the design points were set to coincide with the nodes ($n_{var} = n_{nod}$), but the resulting designs were jagged and thus unrealistic to physically produce, so the number was reduced to one tenth the original number. The number of bits was chosen to create a fine enough resolution without causing an overly long computation time.

Since the target variable of this GA does not necessarily converge to a certain value, an arbitrary limit must be set for the number of generations, n_{gen}, the GA runs before it is terminated. At first, n_{gen} was set to 50, but after finding that large leaps in fitness were happening towards the end of the runs, n_{gen} was extended to 100. This allowed for the impulse to level out somewhat for several generations before the program is terminated. While extending the generations further might result in even higher impulses (and more optimal designs), the computation time would be too high for the purposes of this thesis.

2.4.2 Data Collection

With the parameters decribed in the previous section, the GA was run for various different bearing span angles and target minimum film thicknesses. The span angles, θ, were set to 30, 60, and 90 degrees; and the target minimum film thicknesses (in non-dimensional form), $\frac{h_{min}}{C_0}$, were set to $\frac{1}{20}, \frac{1}{10}, \frac{1}{4}, \text{and} \frac{1}{2}$. For the cylindrical bearing, two $\frac{L}{D}$ ratios were used, 0.5 and 1. For each combination, the program was run three times to generate multiple designs and corresponding maximum impulses. Graphs were generated directly from the data generated by the program using the Matlab plotting tool.

In some cases, the target minimum film thicknesses for all designs was reached immediately after the simulation was started (i.e., on the second time step), which resulted in all chromosomes yielding the same impulse values, which meant that the GA could not work as there was no difference in fitness between the designs. In these cases, the time step was reduced by a factor of 10 from 0.01 s to 0.001 s, after which the GA was able to work properly.

The results for the optimized bearings are compared to those for perfectly spherical and cylindrical bearings as well as bearings with an elliptical profile defined by $C(\theta) = C_0 + \delta \cos^2 \theta$, where δ is the elliptical deviation at the center of the bearing.

The impulses output by the Matlab simulation were confirmed to be in agreement with the impulses given by the analytical solution. An example using a spherical bearing is given below, with the same parameters as the sample case in 3.1.

An analytical formula for calculating the impulse for a perfectly spherical bearing is found in Boedo and Booker [8] and is given by

$$I = \frac{-3\pi R^2 \mu}{(C_0/R)^2}[\ln(1-\epsilon_T) + \frac{\ln(1-\epsilon_T)}{\epsilon_T^2} + \frac{1}{\epsilon_T} + \frac{1}{2}] \quad \text{where} \quad \epsilon_T = 1 - \frac{h_{min}^T}{C_0} \tag{2.39}$$

Using the same parameters as the sample case in the following chapter, $\epsilon_T = 0.95$ and then I evaluates to $43,833$. The impulse calculated by the Matlab simulation in the corresponding scenario was 43,700 (using a 0.01 second time step). This value has a 0.3 percent error from the analytically calculated one.

Chapter 3

Results and Discussion

3.1 Dimensional Studies

A sample dimensional case for a spherical bearing and one for a cylindrical bearing are given below. The dimensional specifications, loading, and fluid properties of the bearings are given in Table 3.1, and the optimized shape and the maximum impulse for each generation are shown in Figures 3.1 and 3.2. For the elliptical profile, the elliptical deviation at the center of the bearing is set to d_{max}, which is the maximum deviation allowed in the GA solution.

Spherical Bearing	
F_0	10,000 N
R	0.025 m
μ	1 $\frac{N-s}{m^2}$
θ_0	90 deg
C_0	20 μm
δ_{max}	20 μm
h_{min}	1 μm

Results	
$I_{optimized}$	733,200 N-s
$I_{spherical}$	43,700 N-s
$I_{elliptical}$	252,200 N-s

Cylindrical Bearing	
F_0	10,000 N
L	0.05 m
D	0.05 m
μ	1 $\frac{N-s}{m^2}$
θ_0	90 deg
C_0	20 μm
δ_{max}	20 μm
h_{min}	1 μm

Results	
$I_{optimized}$	738,900 N-s
$I_{cylindrical}$	37,200 N-s
$I_{elliptical}$	566,500 N-s

Table 3.1: Dimensional and load specifications and results for spherical and cylindrical bearings

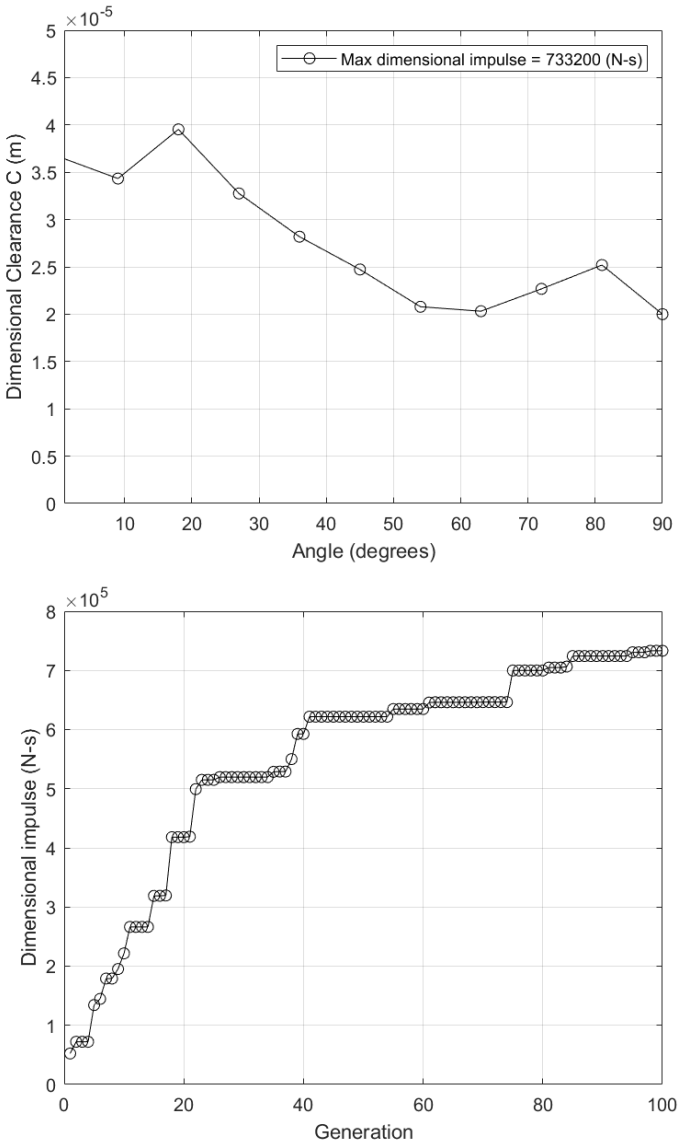

Figure 3.1: Shape profile (top) and maximum impulse for each generation (bottom) of optimized spherical bearing with aforementioned characteristics

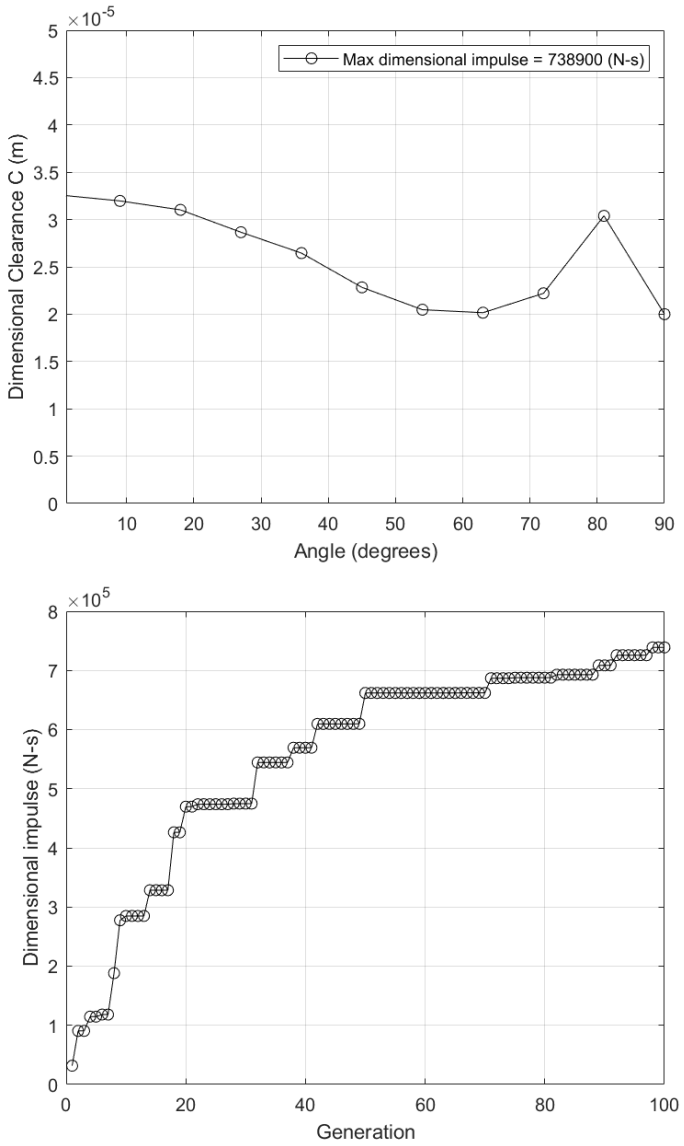

Figure 3.2: Shape profile (top) and maximum impulse for each generation (bottom) of optimized cylindrical bearing with aforementioned characteristics

In both cases, the elliptical profile bearings yielded a far higher impulse than the perfectly spherical and cylindrical bearings, and the optimized bearings yielded an even higher impulse than the elliptical ones. The ratios between the impulse of the optimized and the original bearing are 16.8 (spherical) and 19.9 (cylindrical), an improvement of more than an order of magnitude.

3.2 Non-Dimensional Design Charts

The following chapter contains a selection of results in the form of graphs generated directly from the data using MATLAB. For both spherical bearings and cylindrical bearings, the graphs for the full bearing (90 degree span angle) are shown for all four $\frac{h_{min}}{C_0}$ values, showing the variation in optimized design as the target minimum film thickness increases. The graphs for the partial bearings (60 and 30 degree span angles) are shown for the smallest film thickness, $\frac{h_{min}}{C_0} = \frac{1}{20}$. Then, the 90 degree, $\frac{h_{min}}{C_0} = \frac{1}{20}$ bearing is compared with the corresponding result for the expanded design space ($\delta_{max} = 3C_0$). For the cylindrical bearings, the results for two $\frac{L}{D}$ ratios are compared as well.

3.3 Design Charts: Spherical Bearings

3.3.1 $\frac{\delta_{max}}{C_0} = 1$

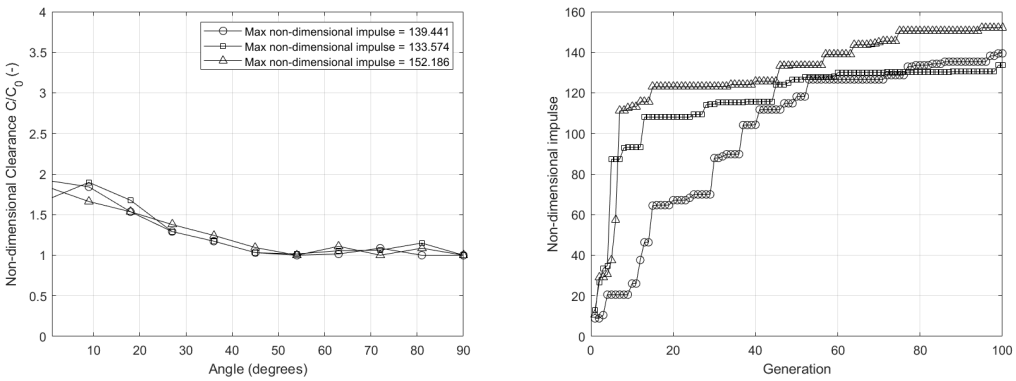

Figure 3.3: Shape profile (L) and maximum impulse for each generation (R) of optimized spherical bearing with 90 degree span angle and $\frac{h^*_{min}}{C_0} = \frac{1}{20}$

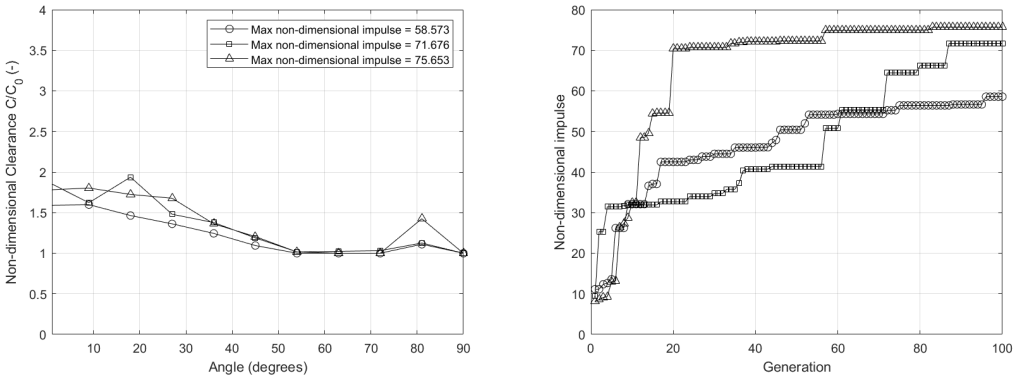

Figure 3.4: Shape profile (L) and maximum impulse for each generation (R) of optimized spherical bearing with 90 degree span angle and $\frac{h^*_{min}}{C_0} = \frac{1}{10}$

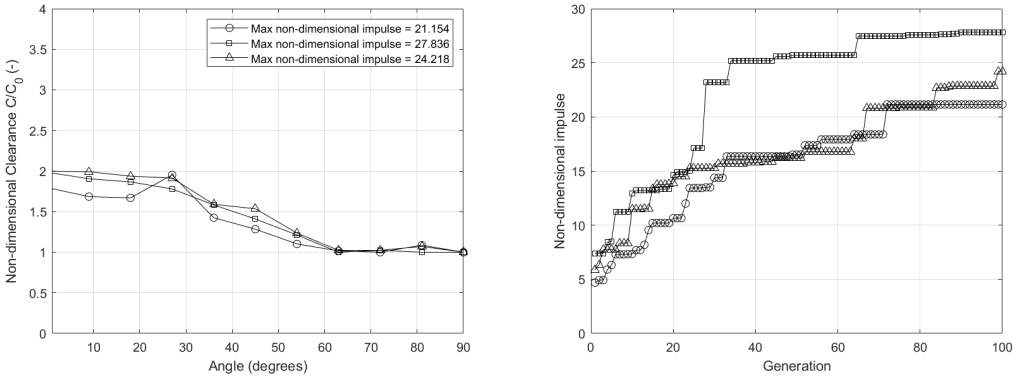

Figure 3.5: Shape profile (L) and maximum impulse for each generation (R) of optimized spherical bearing with 90 degree span angle and $\frac{h^*_{min}}{C_0} = \frac{1}{4}$

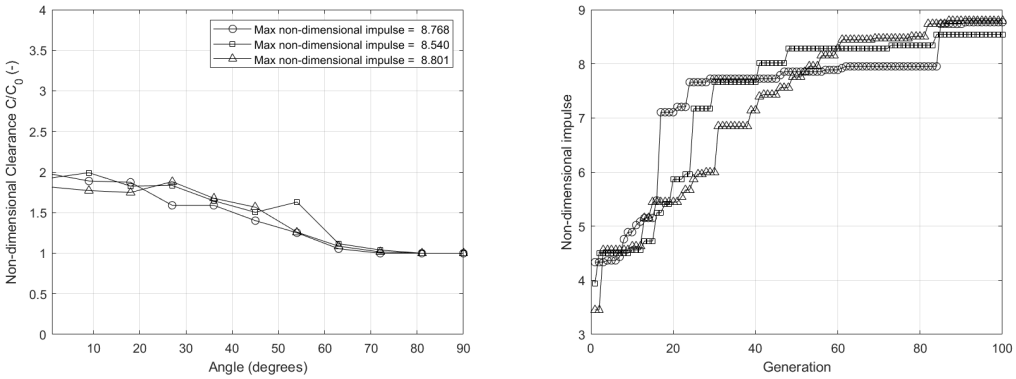

Figure 3.6: Shape profile (L) and maximum impulse for each generation (R) of optimized spherical bearing with 90 degree span angle and $\frac{h^*_{min}}{C_0} = \frac{1}{2}$

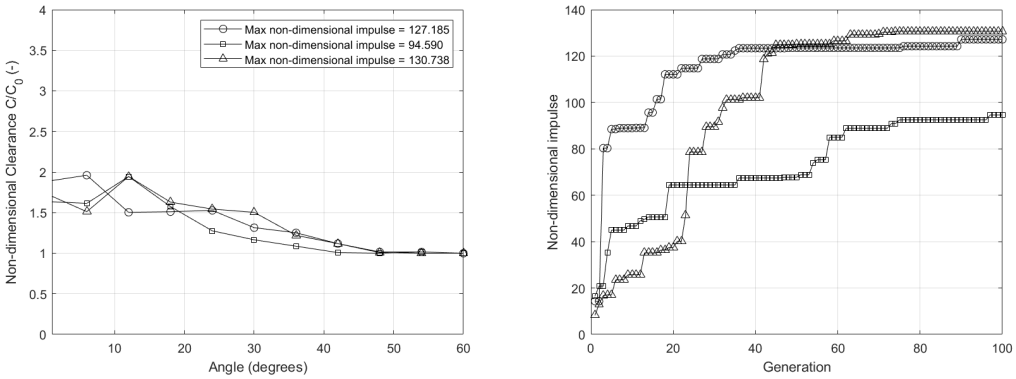

Figure 3.7: Shape profile (L) and maximum impulse for each generation (R) of optimized spherical bearing with 60 degree span angle and $\frac{h^*_{min}}{C_0} = \frac{1}{20}$

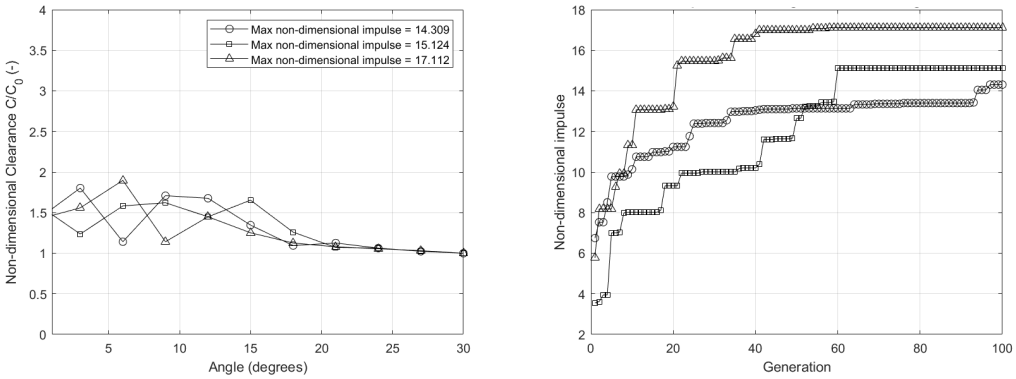

Figure 3.8: Shape profile (L) and maximum impulse for each generation (R) of optimized spherical bearing with 30 degree span angle and $\frac{h^*_{min}}{C_0} = \frac{1}{20}$

3.3.2 $\frac{\delta_{max}}{C_0} = 3$

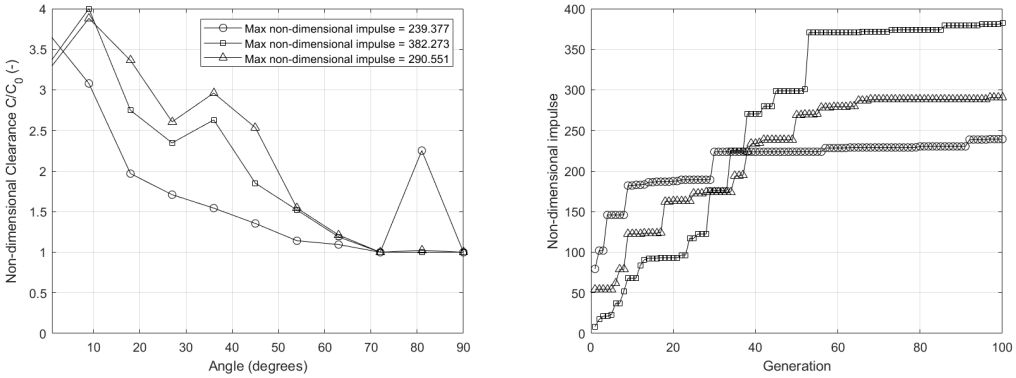

Figure 3.9: Shape profile (L) and maximum impulse for each generation (R) of optimized spherical bearing with 90 degree span angle and $\frac{h^*_{min}}{C_0} = \frac{1}{20}$, with $\delta_{max} = 3C_0$

Spherical Bearing							
Max deviation	Span angle	$\frac{h_{min}}{C_0}$	$\bar{I}_{spherical}$	$\bar{I}_{elliptical}$	$\bar{I}_{optimized}$	$\frac{\bar{I}_{optimized}}{\bar{I}_{spherical}}$	$\frac{\bar{I}_{optimized}}{\bar{I}_{elliptical}}$
$\bar{\delta}_{max} = 1$	90 deg	$\frac{1}{20}$	14.24	82.20	141.73	9.95	1.72
		$\frac{1}{10}$	10.59	44.79	68.63	6.48	1.53
		$\frac{1}{4}$	6.03	19.46	24.40	4.05	1.25
		$\frac{1}{2}$	2.90	9.00	8.70	3.00	0.97
	60 deg	$\frac{1}{20}$	10.07	68.61	117.50	11.67	1.71
		$\frac{1}{10}$	6.75	32.46	53.48	7.93	1.65
		$\frac{1}{4}$	3.13	10.10	11.13	3.56	1.10
		$\frac{1}{2}$	1.21	3.10	2.66	2.21	0.86
	30 deg	$\frac{1}{20}$	3.62	18.79	15.52	4.29	0.83
		$\frac{1}{10}$	1.76	5.36	4.47	2.54	0.83
		$\frac{1}{4}$	0.46	0.86	0.68	1.50	0.80
		$\frac{1}{2}$	0.13	0.19	0.16	1.18	0.82
$\bar{\delta}_{max} = 3$	90 deg	$\frac{1}{20}$	14.24	310.27	304.07	21.35	0.98
		$\frac{1}{10}$	10.59	118.97	102.82	9.71	0.86
		$\frac{1}{4}$	6.03	34.91	30.36	5.03	0.87
		$\frac{1}{2}$	2.90	12.87	13.98	4.82	1.09
	60 deg	$\frac{1}{20}$	10.07	200.72	183.02	18.17	0.91
		$\frac{1}{10}$	6.75	56.98	51.91	7.69	0.91
		$\frac{1}{4}$	3.13	9.42	10.79	3.45	1.15
		$\frac{1}{2}$	1.21	2.15	2.58	2.14	1.20
	30 deg	$\frac{1}{20}$	3.62	6.49	15.21	4.20	2.34
		$\frac{1}{10}$	1.76	2.39	4.19	2.38	1.76
		$\frac{1}{4}$	0.46	0.54	0.66	1.45	1.22
		$\frac{1}{2}$	0.13	0.15	0.14	1.07	0.94

Table 3.2: Results for spherical bearings

3.4 Design Charts: Cylindrical Bearings

3.4.1 $\frac{\delta_{max}}{C_0} = 1, \frac{L}{D} = \frac{1}{2}$

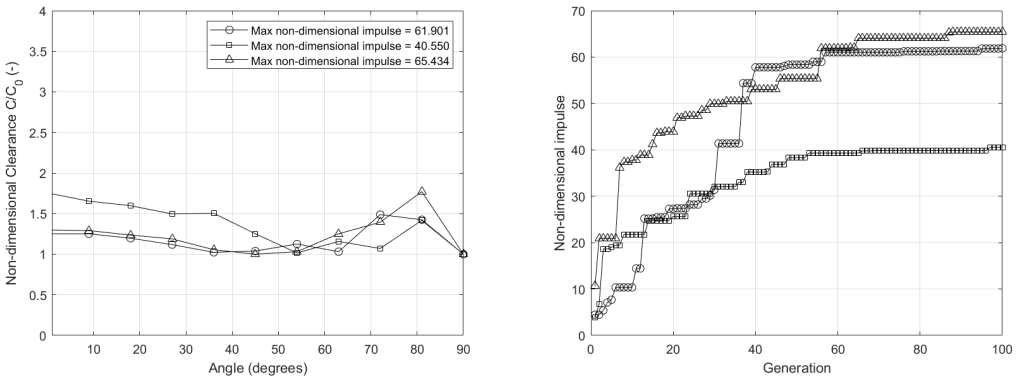

Figure 3.10: Shape profile (L) and maximum impulse for each generation (R) of optimized cylindrical bearing with 90 degree span angle, $\frac{L}{D} = 0.5$ and $\frac{h^*_{min}}{C_0} = \frac{1}{20}$

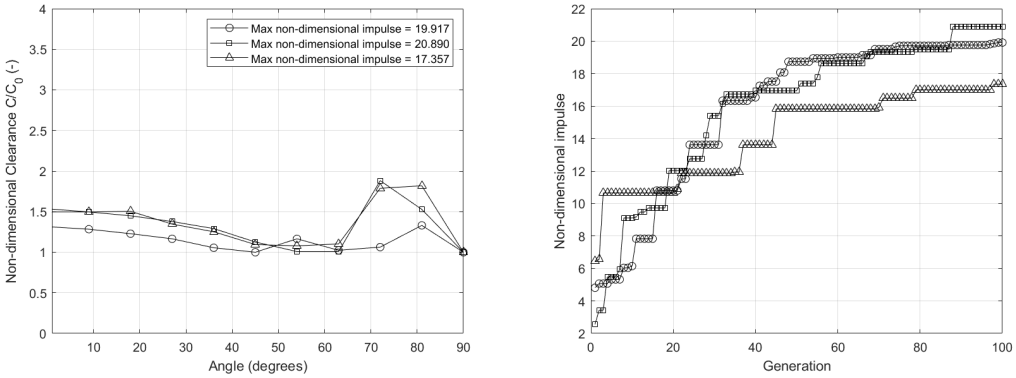

Figure 3.11: Shape profile (L) and maximum impulse for each generation (R) of optimized cylindrical bearing with 90 degree span angle, $\frac{L}{D} = 0.5$ and $\frac{h^*_{min}}{C_0} = \frac{1}{10}$

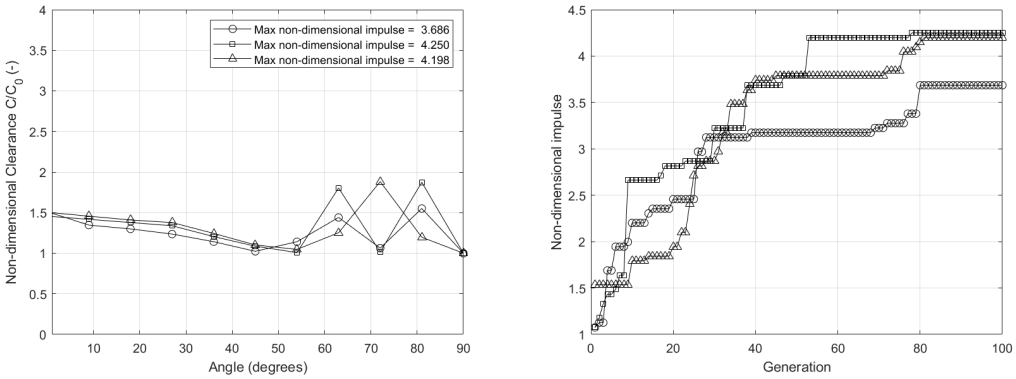

Figure 3.12: Shape profile (L) and maximum impulse for each generation (R) of optimized cylindrical bearing with 90 degree span angle, $\frac{L}{D} = 0.5$ and $\frac{h^*_{min}}{C_0} = \frac{1}{4}$

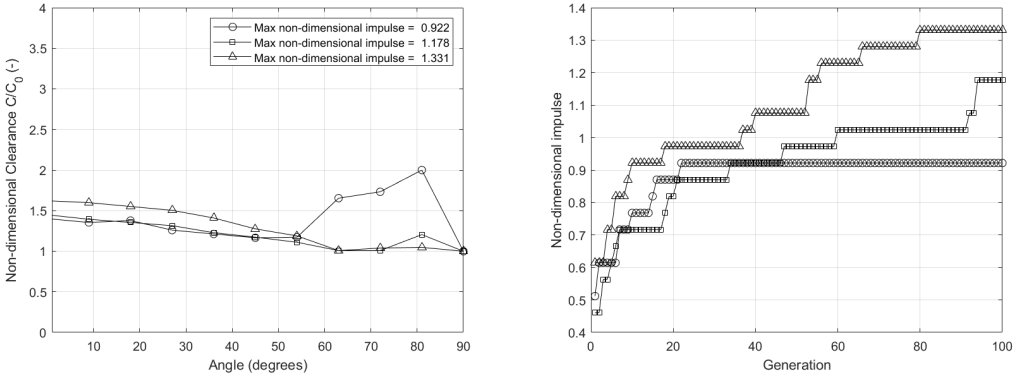

Figure 3.13: Shape profile (L) and maximum impulse for each generation (R) of optimized cylindrical bearing with 90 degree span angle, $\frac{L}{D} = 0.5$ and $\frac{h^*_{min}}{C_0} = \frac{1}{2}$

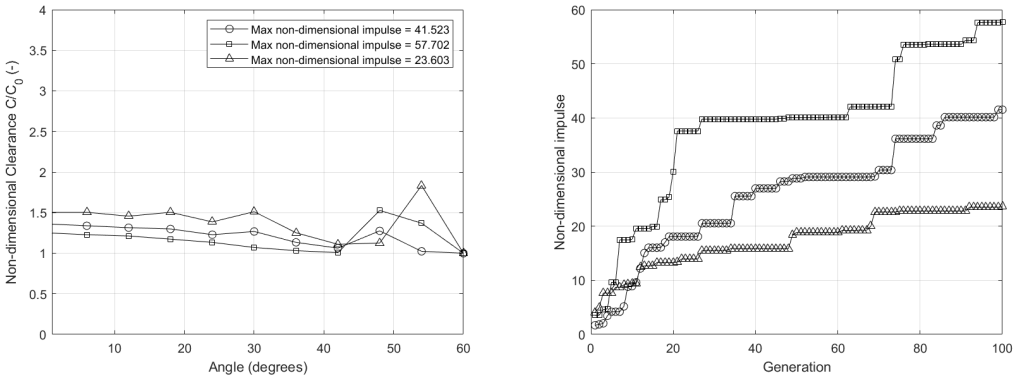

Figure 3.14: Shape profile (L) and maximum impulse for each generation (R) of optimized cylindrical bearing with 60 degree span angle, $\frac{L}{D} = 0.5$ and $\frac{h^*_{min}}{C_0} = \frac{1}{20}$

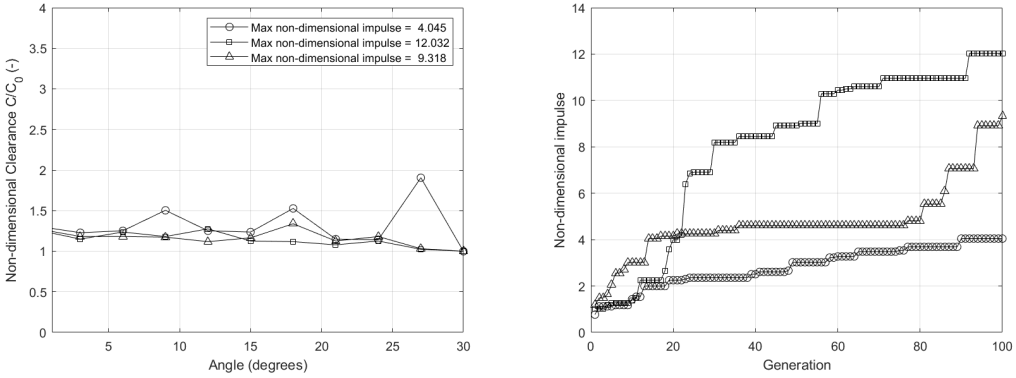

Figure 3.15: Shape profile (L) and maximum impulse for each generation (R) of optimized cylindrical bearing with 30 degree span angle, $\frac{L}{D} = 0.5$ and $\frac{h^*_{min}}{C_0} = \frac{1}{20}$

3.4.2 $\frac{\delta_{max}}{C_0} = 1, \frac{L}{D} = 1$

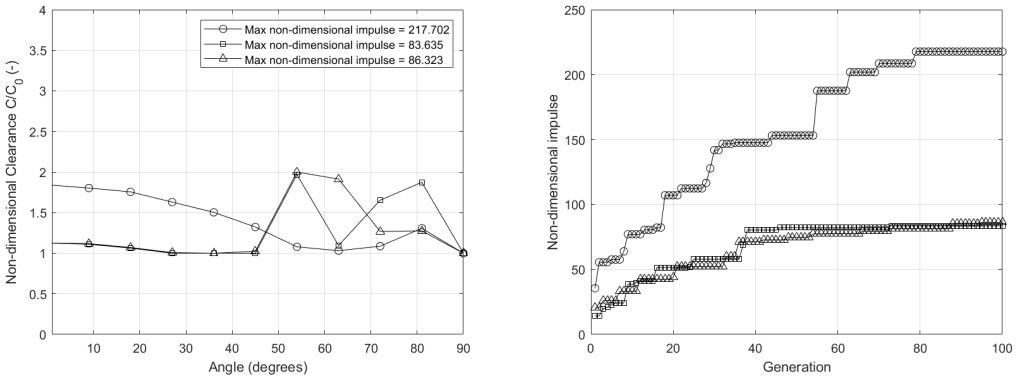

Figure 3.16: Shape profile (L) and maximum impulse for each generation (R) of optimized cylindrical bearing with 90 degree span angle, $\frac{L}{D} = 1$ and $\frac{h^*_{min}}{C_0} = \frac{1}{20}$

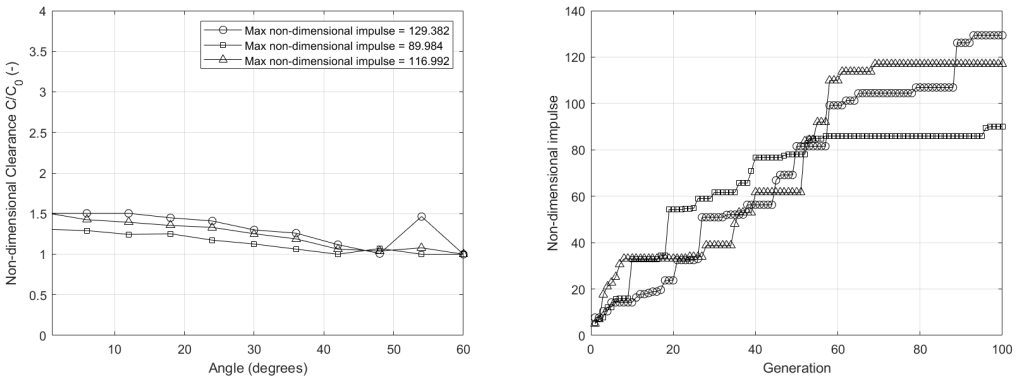

Figure 3.17: Shape profile (L) and maximum impulse for each generation (R) of optimized cylindrical bearing with 60 degree span angle, $\frac{L}{D} = 1$ and $\frac{h^*_{min}}{C_0} = \frac{1}{20}$

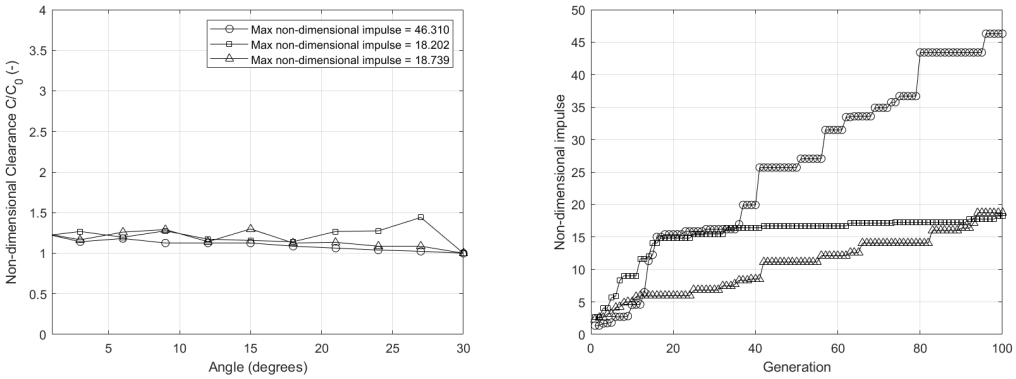

Figure 3.18: Shape profile (L) and maximum impulse for each generation (R) of optimized cylindrical bearing with 30 degree span angle, $\frac{L}{D} = 1$ and $\frac{h^*_{min}}{C_0} = \frac{1}{20}$

3.4.3 $\frac{\delta_{max}}{C_0} = 3, \frac{L}{D} = \frac{1}{2}$

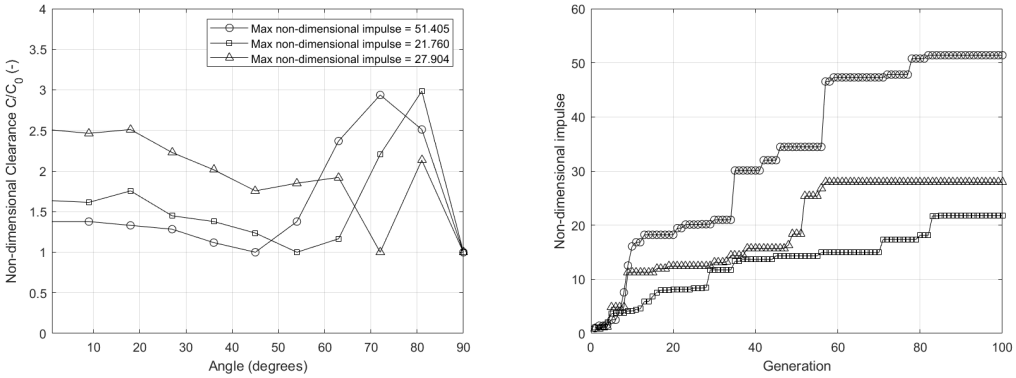

Figure 3.19: Shape profile (L) and maximum impulse for each generation (R) of optimized cylindrical bearing with 90 degree span angle, $\frac{L}{D} = 0.5$ and $\frac{h^*_{min}}{C_0} = \frac{1}{20}$

3.4.4 $\frac{\delta_{max}}{C_0} = 3, \frac{L}{D} = 1$

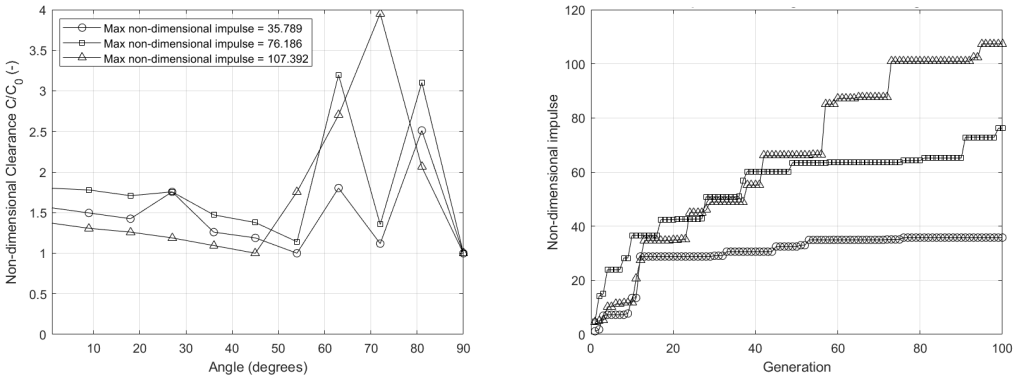

Figure 3.20: Shape profile (L) and maximum impulse for each generation (R) of optimized cylindrical bearing with 90 degree span angle, $\frac{L}{D} = 1$ and $\frac{h^*_{min}}{C_0} = \frac{1}{20}$

Cylindrical Bearing								
Max deviation	$\frac{L}{D}$	Span angle	$\frac{h_{min}}{C_0}$	$\bar{I}_{cylindrical}$	$\bar{I}_{elliptical}$	$\bar{I}_{optimized}$	$\frac{\bar{I}_{optimized}}{\bar{I}_{cylindrical}}$	$\frac{\bar{I}_{optimized}}{\bar{I}_{elliptical}}$
$\bar{\delta}_{max} = 1$	$\frac{1}{2}$	90 deg	$\frac{1}{20}$	19.05	71.27	55.96	2.94	0.79
			$\frac{1}{10}$	9.11	23.86	19.39	2.13	0.81
			$\frac{1}{4}$	2.76	5.02	4.04	1.46	0.81
			$\frac{1}{2}$	0.82	1.23	1.14	1.40	0.93
		60 deg	$\frac{1}{20}$	18.48	69.63	40.94	2.22	0.59
			$\frac{1}{10}$	8.65	22.58	16.13	1.86	0.71
			$\frac{1}{4}$	2.46	4.35	3.35	1.36	0.77
			$\frac{1}{2}$	0.67	1.01	0.85	1.28	0.85
		30 deg	$\frac{1}{20}$	13.57	40.70	8.47	0.62	0.21
			$\frac{1}{10}$	5.43	10.19	5.43	1.00	0.53
			$\frac{1}{4}$	1.18	1.67	0.94	0.80	0.56
			$\frac{1}{2}$	0.30	0.37	0.28	0.93	0.75
	1	90 deg	$\frac{1}{20}$	32.05	145.02	129.22	4.03	0.89
			$\frac{1}{10}$	17.84	56.12	53.67	3.01	0.96
			$\frac{1}{4}$	6.78	14.31	12.26	1.81	0.86
			$\frac{1}{2}$	2.33	4.07	3.69	1.58	0.91
		60 deg	$\frac{1}{20}$	29.49	138.75	112.12	3.80	0.81
			$\frac{1}{10}$	15.64	51.07	35.85	2.29	0.70
			$\frac{1}{4}$	5.38	11.44	8.58	1.60	0.75
			$\frac{1}{2}$	1.66	2.79	2.34	1.41	0.84
		30 deg	$\frac{1}{20}$	18.66	68.33	27.75	1.49	0.41
			$\frac{1}{10}$	7.99	18.59	9.98	1.25	0.54
			$\frac{1}{4}$	1.95	2.90	1.96	1.01	0.68
			$\frac{1}{2}$	0.46	0.64	0.48	1.04	0.74

Table 3.3: Results for cylindrical bearings

Cylindrical Bearing (continued)								
Max deviation	$\frac{L}{D}$	Span angle	$\frac{h_{min}}{C_0}$	$\bar{I}_{cylindrical}$	$\bar{I}_{elliptical}$	$\bar{I}_{optimized}$	$\frac{\bar{I}_{optimized}}{\bar{I}_{cylindrical}}$	$\frac{\bar{I}_{optimized}}{\bar{I}_{elliptical}}$
$\bar{\delta}_{max} = 3$	$\frac{1}{2}$	90 deg	$\frac{1}{20}$	19.05	5.97	33.69	1.77	5.64
			$\frac{1}{10}$	9.11	3.40	9.08	1.00	2.67
			$\frac{1}{4}$	2.76	1.23	3.11	1.12	2.52
			$\frac{1}{2}$	0.82	0.39	0.97	1.19	2.47
		60 deg	$\frac{1}{20}$	18.48	4.04	29.12	1.58	7.21
			$\frac{1}{10}$	8.65	2.23	9.05	1.05	4.06
			$\frac{1}{4}$	2.46	0.76	2.22	0.90	2.91
			$\frac{1}{2}$	0.67	0.25	0.68	1.03	2.72
		30 deg	$\frac{1}{20}$	13.57	3.24	3.96	0.29	1.22
			$\frac{1}{10}$	5.43	1.91	2.39	0.44	1.25
			$\frac{1}{4}$	1.18	0.66	0.63	0.54	0.96
			$\frac{1}{2}$	0.30	0.23	0.21	0.71	0.94
	1	90 deg	$\frac{1}{20}$	32.05	13.40	73.12	2.28	5.46
			$\frac{1}{10}$	17.84	8.68	26.58	1.49	3.06
			$\frac{1}{4}$	6.78	3.60	9.47	1.40	2.63
			$\frac{1}{2}$	2.33	1.25	3.32	1.42	2.66
		60 deg	$\frac{1}{20}$	29.49	9.97	67.31	2.28	6.75
			$\frac{1}{10}$	15.64	6.24	16.08	1.03	2.58
			$\frac{1}{4}$	5.38	2.36	4.18	0.78	1.77
			$\frac{1}{2}$	1.66	0.80	1.31	0.78	1.63
		30 deg	$\frac{1}{20}$	18.66	8.37	20.31	1.09	2.43
			$\frac{1}{10}$	7.99	4.52	7.01	0.88	1.55
			$\frac{1}{4}$	1.95	1.39	1.96	1.01	1.41
			$\frac{1}{2}$	0.46	0.45	0.33	0.72	0.74

Table 3.4: Results for cylindrical bearings (continued)

3.5 Discussion

In addition to the quantitative data that is shown in the figures, some qualitative observations can be made.

Optimized bearings compared to perfectly spherical or cylindrical bearings: For the spherical bearing, the impulse produced by the ball's approach to the optimized bearing was greater than that of the perfectly spherical bearing in all cases. For the cylindrical bearing, this was dependent on span angle. For the largest angle, 90 degrees, the impulse produced by the journal's approach to the optimized bearing was higher than

that of the perfectly cylindrical bearing for 15 of the 16 cases and roughly equal for the remaining one. However, for the reduced bearings (span angles of 60 and 30 degrees), several "optimized" designs had a lower final impulse than the perfectly cylindrical ones (note that the initial shape generated by the algorithm was random, so even though the final shape was in many cases inferior to a perfect cylinder, it was better than the starting random shape in all cases).

Optimized bearings compared to bearings with elliptical profiles: In all cases, the optimized spherical bearings had a smaller advantage over the elliptical ones than over the perfectly spherical ones, and in 12 out of the 24 scenarios examined, had a disadvantage (i.e., lower impulse) than the elliptical bearings. With the cylindrical bearings, there was a distinct difference between the two $\bar{\delta}_{max}$ values. For $\bar{\delta}_{max} = 1$, all optimized bearings were inferior to the elliptical bearings; however, for $\bar{\delta}_{max} = 3$, the optimized bearings were better than the elliptical bearings in 21 out of the 24 cases. This is due to the elliptical bearings with the large deviation having a much lower impulse than the ones with the smaller deviation. This was strangely the opposite of what happened with the spherical bearings, where increasing the elliptical deviation from $\bar{\delta}_{max} = 1$ to 3 resulted in an increase in impulse.

The superiority of many elliptical bearings over their optimized counterparts suggests that eventually, the optimized shape should reach an elliptical profile given enough generations. To see if this was the case, an example where the impulse of the optimized bearing was significantly lower than that of the elliptical profile bearing was selected, and the GA was run for this scenario for 1000 generations instead of 100. The resulting shape (see Figure 3.21), while smoother and having a much smaller bulge than the one generated after 100 generations and thus closer to an elliptical profile, was still not actually elliptical. The final impulse, while higher than that produced by the shorter run, was not as high as the impulse of the elliptical profile bearing, and minimal improvement happened after about 380 generations.

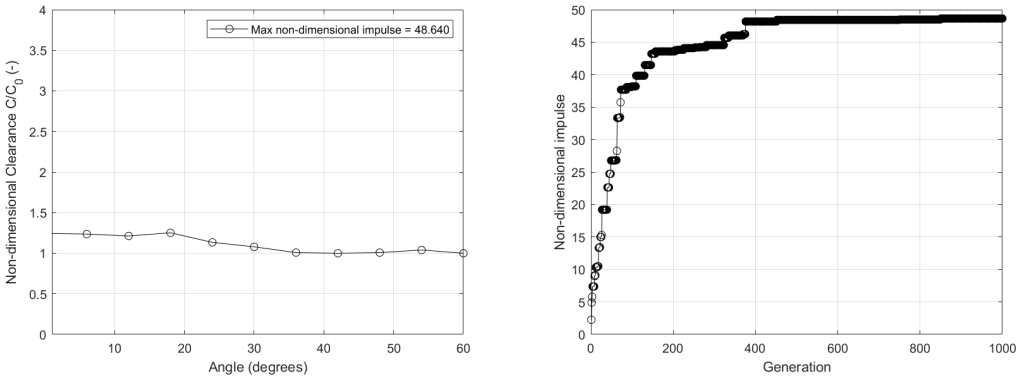

Figure 3.21: Shape profile (L) and maximum impulse for each generation (R) of optimized cylindrical bearing with 60 degree span angle, $\frac{L}{D} = \frac{1}{2}$ and $\frac{h^*_{min}}{C_0} = \frac{1}{20}$, after 1000 generations

The general shape profile of the optimized spherical bearings consists of a larger deviation near the center of the bearing, tapering down towards the edge (extent) of the bearing. In some optimized designs, the maximum deviation is not at the center but at the second or third design point (δ_2 or δ_3), and others have a small spike or "bulge" closer to the edge of the bearing (δ_9 or δ_{10}). When the span angle is reduced to 60 or 30 degrees, the bulge seems to disappear, and the overall profile becomes less "stable" at the smallest span angle (see Figure 3.8).

Like the spherical bearings, the general shape profile of the cylindrical bearings consists of a larger deviation near the center of the bearing ($\theta = 0$), tapering down towards the edge (extent) of the bearing, with the exception of a pronounced spike or "bulge" peaking at the ninth or tenth point (i.e., δ_9 or δ_{10}). While the large bulge was present in most optimized designs, it was less pronounced in a few (see full collection of graphs), with it being the least common and prominent in the 30 degree span bearings.

Expanding the design space in the radial direction from $\delta_{max} = C_0$ to $\delta_{max} = 3C_0$ results in a significant increase in impulse for the spherical bearing, as can be seen in 3.9, but does *not* do the same for the cylindrical bearing (see 3.19 and 3.20). This suggests that in the case of cylindrical bearings, expanding the design space results in less fit designs than those that are generated when the design space is smaller, and 100 generations is not enough for the GA to "fix" the problem.

It is not clear that any single feature contributes to the increrase in impulse from the plain spherical or cylindrical bearing to the optimized one. The designs in which the bulge is absent do not seem to have significantly lower maximum impulses than those that do, and in some examples, like 3.3 and 3.7, nearly identical looking designs have significantly different impulses associated with them, whereas in the example of 3.6, there is little difference in the impulse between the three designs. In the cases of 3.9 and 3.15, the bulge is associated with a lower impulse, although not necessarily the cause of it.

Chapter 4

Conclusion

The results demonstrate the possibility of increasing the impulse produced by the interaction of a ball and cup or journal and sleeve in the case of spherical and cylindrical bearings, respectively, using a genetic algorithm to initiate, evaluate, and create new combinations of designs (i.e., shape profiles) of the inner surface of the bearings. Through this iterative process, the bearing is improved from its initial randomly generated shape over the course of 100 generations into a shape that generally features a bulge towards the center of the bearing and in some cases a steep pocket near the edge. In the case of spherical bearings, the GA consistently produces shapes that are superior to perfectly spherical bearings, but not always superior to bearings with an elliptical profile. In the case of cylindrical journal bearings, the GA often, but not always, produces shapes that are superior to perfectly cylindrical bearings and only in some cases better than journal bearings with an elliptical profile (namely, when the maximum deviation from perfect cylindricity that the GA is allowed to work with is three times the nominal radial clearance and these results are compared to elliptical bearings where the deviation at the center of the bearing is the aforementioned).

In conclusion, between perfectly spherical and cylindrical bearings, bearings with an elliptical profile, and bearings optimized by the GA (given the specific parameters used for this thesis), none of them is unanimously superior, but different ones prevail depending on the specific scenario that is simulated. In the future, further analysis needs to be done to determine the material properties, as well as the machinability, of the geometries produced by the GA.

Appendix A

Finite Element Formuation

A.1 Spherical Geometry

A.1.1 Pressure Fluidity Matrix

General form [18]

$$(\mathrm{K}_{\mathrm{ij}}^{\mathrm{p}})^{\mathrm{e}} = -\int_{\mathrm{A}} \frac{\mathrm{h}^3}{12\mu}(\nabla \mathrm{N_i} \cdot \nabla \mathrm{N_j})\mathrm{dA} \qquad \mathrm{i} = 1,2 \quad \mathrm{j} = 1,2 \tag{A.1}$$

Assuming axisymmetry

$$\mathrm{dA} = 2\pi \mathrm{R}^2 \sin\theta \mathrm{d}\theta \tag{A.2}$$

so that

$$\begin{aligned}(\mathrm{K}_{\mathrm{ij}}^{\mathrm{p}})^{\mathrm{e}} &= -\frac{2\pi \mathrm{R}^2}{12\mu}\int_{\theta_1}^{\theta_2} \frac{\mathrm{h}^3}{\mathrm{R}^2}\frac{\mathrm{dN_i}}{\mathrm{d}\theta}\frac{\mathrm{dN_j}}{\mathrm{d}\theta}\sin\theta \mathrm{d}\theta \\ &\approx -\frac{\pi \sin\bar{\theta}}{6\mu}\int_{\theta_1}^{\theta_2} \mathrm{h}^3 \frac{\mathrm{dN_i}}{\mathrm{d}\theta}\frac{\mathrm{dN_j}}{\mathrm{d}\theta}\mathrm{d}\theta\end{aligned} \tag{A.3}$$

where

$$\bar{\theta} = (\theta_1 + \theta_2)/2 \tag{A.4}$$

Assuming linear shape functions for $\mathrm{N_i}(\theta)$ and assuming $\mathrm{h}(\theta)$ varies linearly within the

element gives [11]

$$\begin{aligned}(\mathrm{K}_{\mathrm{ij}}^{\mathrm{p}})^{\mathrm{e}} &\approx -\frac{\pi \sin\bar{\theta}}{6\mu \mathrm{B}^2}\int_{\theta_1}^{\theta_2} \mathrm{h}^3 \mathrm{b_i b_j dA} \\ &= -\frac{\pi \mathrm{b_i b_j} \sin\bar{\theta}}{24\mu \mathrm{B}}(\sum_{\mathrm{k}=1}^{2} \mathrm{h_k} \sum_{\mathrm{k}=1}^{2} \mathrm{h_k^2})\end{aligned} \tag{A.5}$$

where

$$\mathrm{B} = \theta_2 - \theta_1 \tag{A.6}$$

A.1.2 Squeeze Fluidity Matrix

General form [18]

$$(\dot{\mathrm{K}}_{\mathrm{ij}}^{\mathrm{h}})^{\mathrm{e}} = -\int_{\mathrm{A}} \mathrm{N_i N_j dA} \qquad \mathrm{i} = 1,2 \quad \mathrm{j} = 1,2 \tag{A.7}$$

Assuming axisymmetry

$$\mathrm{dA} = 2\pi \mathrm{R}^2 \sin\theta \mathrm{d}\theta \tag{A.8}$$

so that

$$\begin{aligned}(\dot{\mathrm{K}}_{\mathrm{ij}}^{\mathrm{h}})^{\mathrm{e}} &= -2\pi \mathrm{R}^2 \int_{\theta_1}^{\theta_2} \mathrm{N_i N_j} \sin\theta \mathrm{d}\theta \\ &\approx -2\pi \mathrm{R}^2 \sin\bar{\theta} \int_{\theta_1}^{\theta_2} \mathrm{N_i N_j d}\theta\end{aligned} \tag{A.9}$$

Assuming linear shape functions for $\mathrm{N_i}(\theta)$ gives [11]

$$(\mathrm{K}_{\mathrm{ij}}^{\mathrm{h}})^{\mathrm{e}} = -\frac{\pi \mathrm{R}^2 \mathrm{B} \sin\bar{\theta}}{3}(1 + \delta_{\mathrm{ij}}) \tag{A.10}$$

A.1.3 Area Matrix

Element resultant force is given by

$$\begin{aligned}\mathrm{F}^{\mathrm{e}} &= \int_{\mathrm{A}} \mathrm{p dA} \\ &= 2\pi \mathrm{R}^2 \int_{\theta_1}^{\theta_2} \mathrm{p} \sin\theta \mathrm{d}\theta \\ &\approx 2\pi \mathrm{R}^2 \sin\bar{\theta} \int_{\theta_1}^{\theta_2} \mathrm{p d}\theta\end{aligned} \tag{A.11}$$

Assuming $p(\theta)$ varies linearly within the element gives

$$\begin{aligned} F^e &= 2\pi R^2 \sin\bar{\theta} \int_{\theta_1}^{\theta_2} [p_1 N_1(\theta) + p_2 N_2(\theta)] d\theta \\ &= \pi R^2 p_1 B \sin\bar{\theta} + \pi R^2 p_2 B \sin\bar{\theta} \end{aligned} \tag{A.12}$$

Define nodal forces (positive radially outward) as

$$r_1 = r_2 = \frac{F^e}{2} \tag{A.13}$$

so that

$$r_1 = r_2 = \frac{1}{2}[\pi r^2 p_1 B \sin\bar{\theta} + \pi R^2 p_2 B \sin\bar{\theta}] \tag{A.14}$$

from which we can define an element area matrix

$$(A_{ij})^e = \frac{\pi R^2 B \sin\bar{\theta}}{2} \qquad i = 1,2 \quad j = 1,2 \tag{A.15}$$

A.2 Cylindrical Geometry

The following is taken directly from Boedo [4] and is provided here for completeness.

Given a two-noded element with $h_1, h_2,$ and C_1, C_2 at nodes 1 and 2,

Define for this element

$$\begin{aligned} &< h >= (h_1 + h_2)/2 \\ &< C >= (C_1 + C_2)/2 \\ &s = 1 - \frac{< h >}{< C >} \\ &\lambda = \lambda(s) \\ &\Gamma_1(\frac{\lambda L}{D}), \Gamma_2(\frac{\lambda L}{D}), \Gamma_3(\frac{\lambda L}{D}) \\ &B = R(\theta_2 - \theta_1) \\ &b_1 = -1 \\ &b_2 = +1 \end{aligned} \tag{A.16}$$

A.2.1 Pressure Fluidity Matrix

$$(K_{ij}^{p})^{e} = -\frac{L\Gamma_1}{12\mu B^2} b_i b_j \int_{X_1}^{X_2} h^3 dx - \frac{\Gamma_2}{12\mu L} \int_{X_1}^{X_2} N_i N_j h^3 dx \tag{A.17}$$

where

$$\begin{aligned}
\int_{X_1}^{X_2} h^3 dx &= \frac{B}{4}(h_1 + h_2)(h_1^2 + h_2^2) \\
\int_{X_1}^{X_2} N_1^2 h^3 dx &= \frac{B}{60}(10h_1^3 + 6h_1^2 h_2 + 3h_1 h_2^2 + h_2^3) \\
\int_{X_1}^{X_2} N_2^2 h^3 dx &= \frac{B}{60}(h_1^3 + 3h_1^2 h_2 + 6h_1 h_2^2 + 10h_2^3) \\
\int_{X_1}^{X_2} N_1 N_2 h^3 dx &= \frac{B}{60}(2h_1^3 + 3h_1^2 h_2 + 3h_1 h_2^2 + 2h_2^3)
\end{aligned} \tag{A.18}$$

A.2.2 Squeeze Fluidity Matrix

$$\begin{aligned}
(K_{ij}^{\dot{h}})^{e} &= -L\Gamma_3 \int_{X_1}^{X_2} N_i N_j dx \\
&= -\frac{LB\Gamma_3}{6}(1 + \delta_{ij})
\end{aligned} \tag{A.19}$$

A.2.3 Area Matrix

$$(A_{ij})^{e} = \frac{LB\Gamma_1}{4} \tag{A.20}$$

Bibliography

[1] M. I. Bearings, *Miba Journal Bearing*, 2022.

[2] S. Boedo, *Practical Tribological Issues in Big End Bearings*, Woodhead Publishing Ltd, Cambridge, UK, 2010, pp. 615 – 634.

[3] S. Boedo, *A Computationally Efficient, Mass Conserving Generalized Short Bearing Formulation for Dynamically Loaded Journal Bearings*, ASME Journal of Tribology, 144 (2021). 051802.

[4] S. Boedo, *Mass Conserving Analysis of Steadily Loaded, Oscillating Partial Arc Journal Bearings Using a Generalized Warner Bearing Formulation*, ASME Journal of Tribology, 144 (2022). 101801.

[5] S. Boedo and D. P. Anderson, *Oscillating Journal Bearings Under Steady Load: A Numerical Study of Limiting Cases*, ASME Journal of Tribology, 138 (2015). 014502.

[6] S. Boedo and T. M. Blais, *Revisiting Mobility-Based Predictions of Cyclic Minimum Film Thickness in Big-End Connecting Rod Bearings*, SAE International Journal of Engines, 15 (2022), pp. 263 – 281.

[7] S. Boedo and J. Booker, *Dynamics of Offset Journal Bearings — Revisited*, Proceedings of the Institution of Mechanical Engineers, Part J: Journal of Engineering Tribology, 223 (2009), pp. 359–369.

[8] S. Boedo and J. F. Booker, *A Novel Elastic Squeeze Film Total Hip Replacement*, ASME Journal of Tribology, 136 (2014). 011101.

[9] J. F. Booker, *Squeeze Films and Bearing Dynamics*, CRC Handbook of Lubrication, 2 (1983), pp. 121 – 137.

[10] J. F. Booker, P. K. Goenka, and H. J. van Leeuwen, *Dynamic Analysis of Rocking Journal Bearings With Multiple Offset Segments*, ASME Journal of Lubrication Technology, 104 (1982), pp. 478–487.

[11] J. F. Booker and K. H. Huebner, *Application of Finite Element Methods to Lubrication: An Engineering Approach*, ASME ASME Journal of Lubrication Technology, 94 (1972), pp. 313 – 323.

[12] J. F. Booker and P. Olikara, *Dynamics of Offset Bearings: Parametric Studies*, ASME Journal of Tribology, 106 (1984), pp. 352–358.

[13] R. G. Budynas and J. K. Nisbett, *Shigley's Mechanical Engineering Design (11th Edition)*, McGraw Hill, 2019.

[14] D. Dowson and C. M. Taylor, *A Re-Examination of Hydrosphere Performance*, A S L E Transactions, 10 (1967), pp. 325–333.

[15] A. A. Elsharkawy and L. H. Guedouar, *An Inverse Analysis for Steady-State Elastohydrodynamic Lubrication of One-Layered Journal Bearings*, ASME Journal of Tribology, 122 (1999), pp. 524–533.

[16] S. L. Eshkabilov and S. Boedo, *Optimal Shape Design of Steadily Loaded Journal Bearings Using Genetic Algorithms*, Tribology Transactions, 46 (2003), pp. 134 – 143.

[17] L. M. Gao, Q. E. Meng, F. Liu, J. Fisher, and Z. M. Jin, *The Effect of Aspherical Geometry and Surface Texturing on the Elastohydrodynamic Lubrication of Metal-on-Metal Hip Prostheses under Physiological Loading and Motions*, Proceedings of the Institution of Mechanical Engineers, Part C: Journal of Mechanical Engineering Science, 224 (2010), pp. 2627–2636.

[18] P. K. Goenka and J. F. Booker, *Spherical Bearings: Static and Dynamic Analysis via the Finite Element Method*, ASME Journal of Lubrication Technology, 102 (1980), pp. 308 – 318.

[19] P. K. Goenka and J. F. Booker, *Effect of Surface Ellipticity on Dynamically Loaded Cylindrical Bearings*, ASME Journal of Lubrication Technology, 105 (1983), pp. 1–9.

[20] A. Haraldsson, C. S. Han, H. Tschoepe, and P. Wriggers, *Shape Optimization of a Lubricated Journal Bearing with Regard to the Distribution of Pressure in the Fluid*, Engineering Optimization, 29 (1997), pp. 259–275.

[21] H. Hashimoto, S. Wada, and H. Tsunoda, *Performance Characteristics of Elliptical Journal Bearings in Turbulent Flow Regime*, Bulletin of JSME, 27 (1984), pp. 2265–2271.

[22] M. Häggström, *Hip Prosthesis*, 2022.

[23] Z. M. Jin and D. Dowson, *A Full Numerical Analysis of Hydrodynamic Lubrication in Artificial Hip Joint Replacements Constructed from Hard Materials*, Proceedings of the Institution of Mechanical Engineers, Part C: Journal of Mechanical Engineering Science, 213 (1999), pp. 355–370.

[24] A. Kanarachos, *A Contribution to the Problem of Designing Optimum Performance Bearings*, ASME Journal of Lubrication Technology, 99 (1977), pp. 462–468.

[25] C. J. Maday, *The Maximum Principle Approach to the Optimum One-Dimensional Journal Bearing*, ASME Journal of Lubrication Technology, 92 (1970), pp. 482–487.

[26] Q. E. Meng, F. Liu, J. Fisher, and Z. M. Jin, *Transient Elastohydrodynamic Lubrication Analysis of a Novel Metal-On-Metal Hip Prosthesis with a Non-Spherical Femoral Bearing Surface*, Proceedings of the Institution of Mechanical Engineers, Part H: Journal of Engineering in Medicine, 225 (2011), pp. 25–37. PMID: 21381485.

[27] X. Pang and J. Chen, *Study on 3D Shape Optimization for Hydrodynamic Journal Bearing Using Goal Attainment Multi-Objective Function*, Applied Mechanics and Materials, 319 (2013), pp. 505–509.

[28] X. Pang, J. Chen, and S. Hussain, *Study on Optimization of the Circumferential and Axial Wavy Geometrical Configuration of Hydrodynamic Journal Bearing*, Journal of Mechanical Science and Technology, 27 (2013), pp. 3693–3701.

[29] X. Pang, N. Qin, R. Dwyer-Joyce, J. Chen, and J. Wang, *A General Profile Parameterization of Hydrodynamic Journal Bearings for Efficient Shape Optimization*, Tribology Transactions, 53 (2009), pp. 117–126.

[30] X. Pang, W. Siyuan, and K. Niu, *A Parametric Study of the General Profile for Hydrodynamic Journal Bearings*, Advanced Materials Research, 605-607 (2012), pp. 38–43.

[31] S. M. Rohde, *A Demonstrably Optimum One Dimensional Journal Bearing*, ASME Journal of Lubrication Technology, 94 (1972), pp. 188–192.

[32] C. Shaw and C. Strang, *The Hydrosphere – a New Hydrodynamic Bearing*, Journal of Applied Mechanics, 15 (1948), pp. 137 – 145.

[33] K. Vaidyanathan and T. G. J. Keith, *Numerical Prediction of Cavitation in Noncircular Journal Bearings*, Tribology Transactions, 32 (1989), pp. 215–224.

[34] K. Vaidyanathan and T. G. J. Keith, *Performance Characteristics of Cavitated Noncircular Journal Bearings in the Turbulent Flow Regime*, Tribology Transactions, 34 (1991), pp. 35–44.

[35] Y. Wakuri, S. Ono, and M. Soejima, *On the Lubrication of Crosshead-pin Bearing with Eccentric Journal*, Bulletin of JSME, 25 (1982), pp. 1312–1320.

[36] F. C. Wang, S. X. Zhao, A. F. Quiñonez, H. Xu, X. S. Mei, and Z. M. Jin, *Nonsphericity of Bearing Geometry and Lubrication in Hip Joint Implants*, ASME Journal of Tribology, 131 (2009). 031201.

[37] L. Wang, H. Geng, W. Zhang, X. Ge, and M. He, *Effect of Ellipticity on Cavitation Mechanism and Thermal Effect of Elliptical Journal Bearings*, Tribology Online, 16 (2021), pp. 279–285.

[38] N. Wang, C.-L. Ho, and K.-C. Cha, *Engineering Optimum Design of Fluid-Film Lubricated Bearings*, Tribology Transactions, 43 (2000), pp. 377–386.

[39] P. C. Warner, *Static and Dynamic Properties of Partial Journal Bearings*, Journal of Basic Engineering, 85 (1963), pp. 247–255.